SKYFALL-GS: SYNTHESIZING IMMERSIVE 3D URBAN SCENES FROM SATELLITE IMAGERY

Anonymous authors
Paper under double-blind review

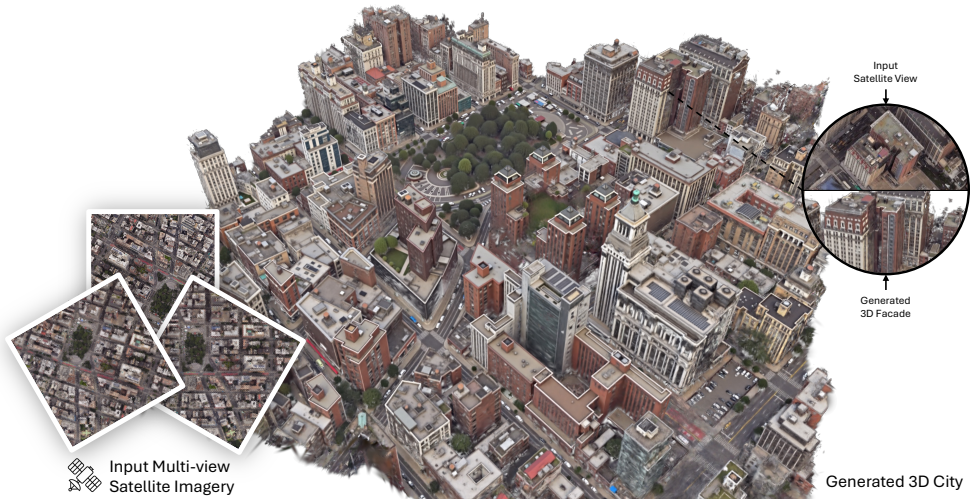

Figure 1: **Our method synthesizes high-quality, immersive 3D urban scenes solely from multi-view satellite imagery, enabling realistic drone-view navigation without relying on additional 3D or street-level training data.** Given multiple satellite images from diverse viewpoints and dates (*left*), our method leverages 3D Gaussian Splatting combined with pre-trained text-to-image diffusion models in an iterative refinement framework to generate realistic 3D block-scale city from limited satellite-view input (*right*). Our method significantly enhances visual fidelity, geometric sharpness, and semantic consistency, enabling real-time immersive exploration.

ABSTRACT

Synthesizing large-scale, explorable, and geometrically accurate 3D urban scenes is a challenging yet valuable task in providing immersive and embodied applications. The challenges lie in the lack of large-scale and high-quality real-world 3D scans for training generalizable generative models. In this paper, we take an alternative route to create large-scale 3D scenes by synergizing the readily available satellite imagery that supplies realistic coarse geometry and the open-domain diffusion model for creating high-quality close-up appearances. We propose **Skyfall-GS**, a novel hybrid framework that synthesizes immersive city-block scale 3D urban scenes by combining satellite reconstruction with diffusion refinement, eliminating the need for costly 3D annotations, also featuring real-time, immersive 3D exploration. We tailor a curriculum-driven iterative refinement strategy to progressively enhance geometric completeness and photorealistic textures. Extensive experiments demonstrate that Skyfall-GS provides improved cross-view consistent geometry and more realistic textures compared to state-of-the-art approaches.

1 INTRODUCTION

Synthetic high-quality, immersive, and semantically plausible 3D urban scenes have crucial applications in gaming, filmmaking, and robotics. The ability to create a large-scale and 3D-grounded environment supports realistic rendering and immersive experience for storytelling, demonstration, and embodied physics simulation. However, due to limited 3D-informed data, building a generative

model for realistic and navigable 3D cities remains challenging. It is expensive and labor-intensive to acquire large-scale 3D and textured reconstructions of cities with detailed geometry, while using Internet image collections face challenges in camera pose registration and excessive data noise (e.g., transient objects and different times of the day). These constraints set back existing 3D city generation frameworks from creating realistic and diverse appearances. With this observation, we propose an alternative route for virtual city creation with a two-stage pipeline: partial and coarse geometry reconstruction from multi-view satellite imagery, then close-up appearance completion and hallucination using an open-domain diffusion model.

Satellite imagery offers a compelling alternative due to its extensive geographic coverage, automated collection, and high-resolution capabilities. For instance, Maxar's WorldView-3 satellite captures approximately 680,000 km^2 of imagery daily at resolutions up to 31 cm per pixel. Such data inherently encodes semantically plausible representations of real-world environments, enabling scalable 3D urban scene creation. However, in Figure 2(a), we show that directly applying 3D reconstruction methods to satellite imagery is insufficient for creating *navigable and immersive* 3D cities. The significant amount of invisible regions (e.g., building facades) and limited satellite-view parallax create incorrect geometry and artifacts.

Completing and enhancing the geometry and texture in the ground view requires a significant influx of extra information. In Figure 2(b), we study a few state-of-the-art methods in city generation (Xie et al., 2024; 2025b). These methods produce oversimplified building geometries and unrealistic appearances due to strong assumptions, particularly the reliance on semantic maps and height fields as the sole inputs, and overfitting to small-scale, domain-specific datasets. Such an observation motivates us to seek help from open-domain foundation vision models as an external information source, which provides better zero-shot generalization and diversity. Noticing that the ground-view novel-view renderings from the GS reconstructed scene exhibit noise-like patterns, we treat these renderings as intermediate results in a denoising diffusion process. Then, we complete the remaining denoising process to create hallucinated pseudo ground-truth for the GS scene optimization. To stabilize the convergence, we carefully design a curriculum-based view selection and iterative refinement process, where the sampled view angles gradually *fall* from the *sky* to the ground over time. Accordingly, we name our framework **Skyfall-GS**. In Figure 1 and Figure 2, we show that Skyfall-GS yields significantly enhanced texture with 3D-justified geometry compared to the relevant baselines.

Skyfall-GS is a novel hybrid framework that synthesizes immersive city-block scale 3D urban scenes by combining satellite reconstruction with diffusion refinement, eliminating the need of fixed-domain training on 3D data. Skyfall-GS operates on readily available satellite imagery as the only input, then hallucinates realistic aerial-view appearances and maintains a strong satellite-to-ground 3D consistency. Moreover, Skyfall-GS supports real-time and interactive rendering, as we design our framework to produce GS results without sophisticated data structures. Through experiments on diverse environments, we show that Skyfall-GS has better generalization and robustness compared to state-of-the-art methods. Our ablation shows that each of our designs improves the perceptual plausibility and semantic consistency. Skyfall-GS paves the way for scalable 3D urban virtual scene creation, enabling applications in virtual entertainment, simulation, and robotics.

In summary, our contributions include:

- We introduce Skyfall-GS, the first method to synthesize immersive, real-time free-flight navigable 3D urban scenes solely from multi-view satellite imagery using generative refinement.
- An open-domain refinement approach leveraging pre-trained text-to-image diffusion models without domain-specific training.
- A curriculum-learning-based iterative refinement strategy progressively enhances reconstruction quality from higher to lower viewpoints, significantly improving visual fidelity in occluded areas.

2 Related Work

Gaussian Splatting. 3D Gaussian Splatting (3DGS) (Kerbl et al., 2023) offers real-time view synthesis rivaling NeRFs (Mildenhall et al., 2021; Barron et al., 2021; 2022; Müller et al., 2022; Barron et al., 2023; Martin-Brualla et al., 2021). Mip-Splatting (Yu et al., 2024) fixes scale-change issues via on-the-fly resizing. Recent advances target satellite and aerial reconstruction: FusionRF (Sprintson et al., 2024) achieves 17% depth improvement from multispectral acquisitions, while InstantSplat (Fan et al., 2024) enables 40-second pose-free reconstruction. "In-the-wild" vari-

Figure 2: **Limitations of existing novel-view synthesis methods from satellite imagery.** (a) Sat-NeRF (Marí et al., 2022) and naive 3DGS (Kerbl et al., 2023) yield blurred or distorted building facades due to insufficient geometric detail and limited parallax from satellite viewpoints. (b) City generation methods (Xie et al., 2024; 2025b) produce oversimplified building geometries and unrealistic appearances, primarily due to strong assumptions about the input data, and overfitting to small-scale, domain-specific datasets. In comparison, our method synthesizes more realistic appearances and geometries from aerial views.

ants handle appearance and uncertainty (Xu et al., 2024; Sabour et al., 2024; Wang et al., 2024b; Dahmani et al., 2024; Zhang et al., 2024a; Kulhanek et al., 2024; Hou et al., 2025), including SpectroMotion (Fan et al., 2025) for dynamic specular scenes, while large-scene methods use LOD and partitioning (Kerbl et al., 2024; Liu et al., 2025c; 2024; Lin et al., 2024; Turki et al., 2022; Tancik et al., 2022). CAT-3DGS (Zhan et al., 2025) achieves rate-distortion optimization via context-adaptive triplanes. For sparse-view satellite imagery, depth or co-regularization priors guide reconstruction (Li et al., 2024b; Zhang et al., 2024b; Zhu et al., 2023; Niemeyer et al., 2022; Lin et al., 2025), with SparseSat-NeRF (Zhang & Rupnik, 2023) adding dense depth supervision.

Diffusion models for 3D reconstruction and editing. Diffusion models (Rombach et al., 2022; Labs, 2024b) underpin image generation and editing. Early SDS pipelines DreamFusion (Poole et al., 2022) and Magic3D (Lin et al., 2023a) enabled text-to-3D, with ProlificDreamer (Wang et al., 2023) addressing over-smoothing via Variational Score Distillation. DreamGaussian (Tang et al., 2023) achieves 10x speedup via progressive densification, while GaussianDreamer (Yi et al., 2024) bridges 2D and 3D diffusion models. SDEdit (Meng et al., 2022), DDIM inversion (Mokady et al., 2022; Miyake et al., 2024), and FlowEdit (Kulikov et al., 2024) enable fine control. Extensions include sparse-view reconstruction (Wu et al., 2023; Liu et al., 2023b; Chen et al., 2024), with MVDream (Shi et al., 2023) enabling multi-view consistency. For 3D/4D generation (Gao et al., 2024b; Wu et al., 2024b; Melas-Kyriazi et al., 2024; Chung et al., 2023; Liu et al., 2023a) and scene editing (Haque et al., 2023; Wu et al., 2025; Ye et al., 2024b; Fang et al., 2024; Mirzaei et al., 2024; Dihlmann et al., 2024; Weber et al., 2024; Wu et al., 2024a; Wang et al., 2025), SPIn-NeRF (Mirzaei et al., 2023) handles occlusions via perceptual inpainting while CF-NeRF (Shen et al., 2022) provides uncertainty quantification. CorrFill (Liu et al., 2025a) enhances faithfulness via correspondence guidance, while AuraFusion360 (Wu et al., 2025) enables 360° scene inpainting for Gaussian Splatting. Instruct-NeRF2NeRF (Haque et al., 2023) refines NeRF views iteratively with Instruct-Pix2Pix (Brooks et al., 2023) for diffusion-driven 3D editing.

Urban scene modeling. Classic SfM-MVS pipelines extract DSMs from satellite pairs (Schönberger & Frahm, 2016; Zhang et al., 2019; Gao et al., 2023a), with MVS3D (Bosch et al., 2016) benchmarks for evaluation. Neural variants improve geometric fidelity (Derksen & Izzo, 2021; Marí et al., 2022; 2023; Zhou et al., 2024b; Leotta et al., 2019; Liu et al., 2025b; Qu & Deng, 2023; Gao et al., 2024a; Savant Aira et al., 2025; Huang et al., 2025), including Sat-NeRF (Marí et al., 2022), which utilizes NeRF for satellite imagery and SatMVS (Gao et al., 2021; 2023b) with RPC warping, yet both miss occluded facades. Generative synthesis divides into: (i) street-view methods (Li et al., 2024c; 2021; 2024d; Toker et al., 2021; Qian et al., 2023; Shi et al., 2022; Ze et al., 2025; Deng et al., 2024; Xu & Qin, 2025), including GeoDiffusion (Xiong et al., 2024) for mixed-view synthesis, Geospecific View Generation (Xu & Qin, 2024) achieving 10x resolution gains, and SkyDiffusion (Ye et al., 2024a) with Curved-BEV for street-to-satellite mapping, though lacking 3D consistency and temporal coherence; and (ii) full-3D city generation (Lin et al., 2023b; Xie et al., 2024; 2025a;b; Sun et al., 2024; Zhou et al., 2024a; Shang et al., 2024; Li et al., 2024a; Zhang et al., 2024c), with BEVFormer (Li et al., 2022) and MagicDrive (Gao et al., 2023c) using spatiotemporal transformers for view consistency. While Infinicity (Lin et al., 2023b) uses pixel-to-voxel rendering for infinite cities, and CityDreamer (Xie et al., 2024) and GaussianCity (Xie et al., 2025b) use BEV neural fields or BEV-Point splats for editable scenes, these remain constrained by input representations (semantic maps and height fields) and training distributions, limiting synthesis of realistic textures and complex structures like tunnels, bridges, and multi-level architectures. Our method uses pretrained diffusion priors to recover

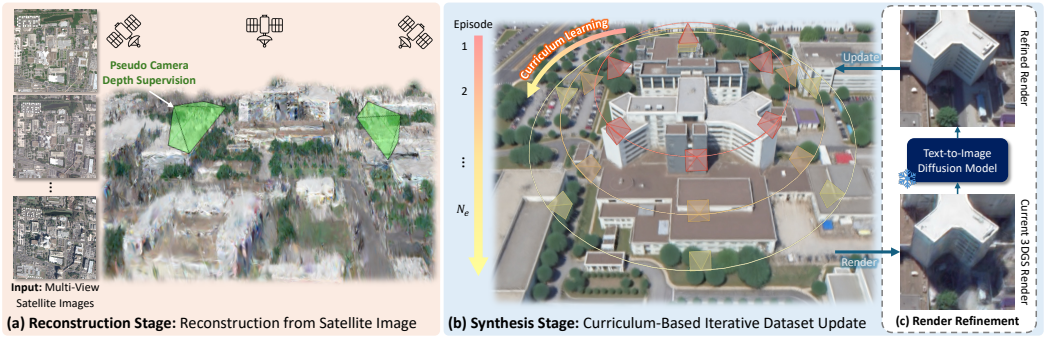

Figure 3: **Overview of the proposed Skyfall-GS pipeline.** Our method synthesizes immersive and free-flight navigable city-block scale 3D scenes solely from multi-view satellite imagery in two stages. (a) In the Reconstruction Stage, we first reconstruct the initial 3D scene using 3DGS, enhanced by pseudo-camera depth supervision to address limited parallax in satellite images. We use an appearance modeling component to handle varying illumination conditions across multi-date satellite images. (b) In the Synthesis Stage, we introduce a curriculum-based Iterative Dataset Update (IDU) refinement technique leveraging (c) a pre-trained T2I diffusion model (Labs, 2024b) with prompt-to-prompt editing (Kulikov et al., 2024). By iteratively updating training datasets with progressively refined renders, our approach significantly reduces visual artifacts, improving geometric accuracy and texture realism, particularly in previously occluded areas such as building facades.

high-fidelity facades in occluded regions without dataset-specific training, respecting user constraints more faithfully.

3 METHOD

Our two-stage pipeline (Figure 3) turns satellite images into immersive 3D cities. Reconstruction Stage (Section 3.1): fit a 3D Gaussian Splatting model, adding illumination-adaptive appearance modeling and regularizers for sparse, multi-date views. Synthesis Stage (Section 3.2): recover occluded regions, e.g., facades, through curriculum Iterative Dataset Update, repeatedly refining renders with text-guided diffusion edits. The loop keeps textures faithful to the satellite input while preserving geometry, yielding complete, navigable urban scenes from satellite data alone.

Preliminary. 3D Gaussian Splatting (3DGS) (Kerbl et al., 2023) encodes a scene as Gaussians with center μ_i, covariance Σ_i, opacity α_i, and view-dependent color. Each Gaussian projects to the image plane with covariance: $\Sigma_i' = JW\Sigma_i W^T J^T$, where W is the viewing transformation and J is the affine-projection Jacobian. Pixels are alpha-composited front-to-back. Parameters are trained with:

$$\mathcal{L}_{\text{color}} = \lambda_{\text{D-SSIM}}\,\text{DSSIM}(\hat{C}, C) + (1 - \lambda_{\text{D-SSIM}})\|\hat{C} - C\|_1 \ . \tag{1}$$

3.1 INITIAL 3DGS RECONSTRUCTION FROM SATELLITE IMAGERY

The initial 3DGS reconstruction must faithfully preserve the texture and geometry of satellite imagery to provide a robust foundation for synthesis. We employ appearance modeling to handle variations in multi-date imagery. Since limited satellite parallax creates floating artifacts, we apply regularization techniques to constrain both texture and geometry.

Approximated camera parameters. Satellite imagery typically uses the rational polynomial camera (RPC) model, directly mapping image coordinates to geographic coordinates. To integrate with the 3DGS pipeline, we employ SatelliteSfM (Zhang et al., 2019) to approximate perspective camera parameters (extrinsic and intrinsic) from RPC and generate sparse SfM points as initial 3DGS points.

Appearance modeling. As highlighted in Section 1, multi-date satellite imagery exhibits significant appearance variations due to global illumination changes, seasonal factors, and transient objects, as illustrated in Figure 3(a). Following WildGaussians (Kulhanek et al., 2024), we use trainable per-image embeddings $\{e_j\}_{j=1}^N$ (with N training images) to handle varying illumination and atmospheric conditions. We also employ trainable per-Gaussian embeddings g_i to capture localized appearance changes like shadow variations. A lightweight MLP f computes affine color transformation parameters (β, γ) as $(\beta, \gamma) = f(e_j, g_i, \bar{c}_i)$, where e_j is the per-image embedding, g_i is the per-Gaussian embedding, and $\bar{c}_i$ denotes the 0-th order spherical harmonics (SH). Finally, the transformed color $\tilde{c}_i$

is then computed as $\tilde{c}_i(\mathbf{r}) = \gamma \cdot \hat{c}_i(\mathbf{r}) + \beta$, and used in the 3DGS rasterizer. To prevent modeling the appearance changes as view-dependent effects, we limit SH to zero and first-order terms.

Opacity regularization. We observed that numerous floaters in reconstructed scenes exhibit low opacity. To encourage geometry to adhere closely to actual surfaces, we propose entropy-based opacity regularization:

$$\mathcal{L}_{\text{op}} = -\sum_i \alpha_i \log(\alpha_i) + (1-\alpha_i)\log(1-\alpha_i) \ . \tag{2}$$

This regularization promotes binary opacity distributions, allowing low-opacity Gaussians to be pruned during densification. Incorporating this term significantly sharpens geometric reconstruction, providing a better foundation for subsequent synthesis.

Pseudo camera depth supervision. To further reduce floating artifacts, we sample pseudo-cameras positioned closer to the ground during optimization. From these pseudo-cameras, we render RGB images I_{RGB} and corresponding alpha-blended depth maps $\hat{D}_{\text{GS}}$. We then use an off-the-shelf monocular depth estimator, MoGe (Wang et al., 2024a), to predict scale-invariant depths $\hat{D}_{\text{est}}$ from these renders. We use the absolute value of Pearson correlation (PCorr) to supervise the depth:

$$\mathcal{L}_{\text{depth}} = \|\text{PCorr}(\hat{D}_{\text{GS}}, \hat{D}_{\text{est}})\|_1 \ ; \quad \text{PCorr}(\hat{D}_{\text{GS}}, \hat{D}_{\text{est}}) = \frac{\text{Cov}(\hat{D}_{\text{GS}}, \hat{D}_{\text{est}})}{\sqrt{\text{Var}(\hat{D}_{\text{GS}})\text{Var}(\hat{D}_{\text{est}})}} \ . \tag{3}$$

Optimization. Combining all components, the overall loss for the reconstruction stage is defined as:

$$\mathcal{L}_{\text{sat}}(G, C) = \mathcal{L}_{\text{color}} + \lambda_{\text{op}}\mathcal{L}_{\text{op}} + \lambda_{\text{depth}}\mathcal{L}_{\text{depth}} \ , \tag{4}$$

where G is the 3DGS representation, C is the set of ground-truth satellite images, λ_{op} and λ_{depth} weight opacity regularization and depth supervision relative to the color reconstruction loss.

3.2 Synthesize via Curriculum-learning Based Iterative Datasets Update

The iterative dataset update (IDU) technique (Haque et al., 2023; Melas-Kyriazi et al., 2024) repeatedly executes render-edit-update cycles across multiple episodes to progressively synthesize 3D scenes. Unlike previous methods that sample camera poses from original training views (Haque et al., 2023) or simple orbits (Melas-Kyriazi et al., 2024), we introduce a curriculum-based refinement schedule over N_e episodes that specifically addresses satellite imagery's geometric and visual limitations, producing structurally accurate and photorealistic reconstructions of occluded areas.

Curriculum learning strategy. As illustrated in Figure 4, we observe that 3DGS trained from satellite imagery produces higher-quality renders at higher elevation angles but degenerates at lower elevation angles. Leveraging this insight, we introduce a curriculum-based synthesizing strategy, which progressively lowering viewpoints across optimization episodes. Specifically, we define N_p look-at points $\{P_i\}_{i=1}^{N_p}$ uniformly placed throughout the scene and uniformly sample N_v camera positions along orbital trajectories with controlled elevation angles and radii. Our iterative dataset update (IDU) process starts from higher elevations, progressively moving toward lower perspectives. This approach gradually reveals previously occluded regions, improving geometric detail and texture realism, as validated in our ablation studies (Section 4.2).

Render refinement by text-to-image diffusion model. As illustrated in Figure 5(a), renderings from initial 3DGS contain blurry texture and artifacts. To address this, we leverage prompt-to-prompt editing with pre-trained text-to-image diffusion models to synthesize disocclusion areas, remove artifacts, and enhance geometry. Prompt-to-prompt editing (Hertz et al., 2022) modifies input images, which are described by the source prompt, to align with the target prompt while preserving structural content. Although typically used on real or diffusion-generated photos, we demonstrate its effectiveness for refining degraded satellite-trained 3DGS renders. We employ FlowEdit (Kulikov et al., 2024) with the pre-trained `FLUX.1 [dev]` diffusion model (Labs, 2024a), using prompt pairs that transform degenerate renders into high-quality imagery. Our prompts specifically describe the degraded features in original renders and specify the desired high-quality attributes in target prompts, see Section A.1 for prompts detail. As illustrated in Figure 5, this approach significantly improves the visual quality of renders, including sharper geometric details, enhanced texture richness, and physically coherent shadows, strengthening the 3DGS training dataset for more accurate reconstructions.

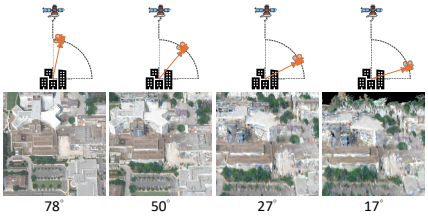

Figure 4: **The motivation of curriculum strategy.** Renderings of the initial 3D reconstruction from varied elevation angles reveal progressive degradation as the viewing angle decreases.

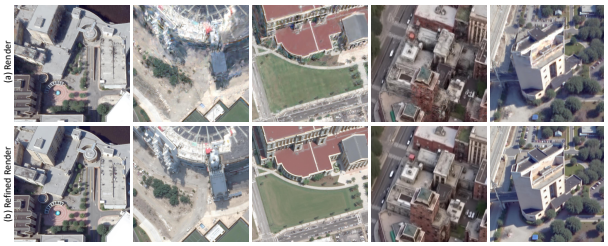

Figure 5: **Render refinement.** (a) Original 3DGS render with artifacts and blurry textures; (b) Refined result showing enhanced geometry and texture quality.

Multiple diffusion samples. While diffusion models effectively refine individual 3DGS renders, independently applying them across viewpoints introduces inconsistencies. Furthermore, 3DGS is well known to suffer from overfitting on single views, as pointed out by CoR-GS (Zhang et al., 2024b), causing artifacts when rendering from novel viewpoints.

Ideally, the optimal denoising diffusion process should produce a distribution where all views maintain synchronized 3D appearance. However, independent 2D denoising on each view does not preserve 3D consistency, resulting in a denoising trajectory distribution that is a super-set of the optimal trajectories. Selecting a single denoising trajectory from this expanded distribution has negligible probability of yielding the optimal 3D-consistent result, leading to the artifacts observed in Figure 9(c).

To mitigate this, we synthesize N_s independently refined samples per view, effectively sampling multiple trajectories from the denoising distribution. During optimization, the photometric loss $\mathcal{L}_{\text{color}}$ implicitly averages over these N_s samples. Rather than committing to a single potentially suboptimal denoising path, this approach allows the 3DGS optimization to find a consensus representation that balances fidelity to individual samples while promoting geometric coherence across views. Ablation studies (Section 4.2) and Figure 9(c) confirm that this strategy successfully balances detail preservation with structural coherence.

Iterative dataset update. Our curriculum-based Iterative Dataset Update (IDU), detailed in Algorithm 1, optimizes the 3DGS over N_e episodes. In each episode, we render curriculum-guided views and refine them using FlowEdit (Kulikov et al., 2024) with specified prompts and strengths to generate a new training set. As the curriculum descends to lower altitudes, rendering quality steadily improves, particularly in previously occluded regions, as illustrated in Figure 6. We provide detailed parameters in Section A.1.

Algorithm 1 3DGS Refinement via Iterative Dataset Updates

Input: N_e: Number of episodes
Input: N_v, N_s, N_p: Number of views per point, samples per view and look-at points
Input: $\{P_i\}_{i=1}^{N_p}$: A set of N_p target look-at points
Input: $\{R_i\}_{i=1}^{N_e}, \{E_i\}_{i=1}^{N_e}$: Decreasing sequences for radius and elevation with lengths of N_e
Input: T_{src}, T_{tgt}, $n_{\min}$, $n_{\max}$: FlowEdit parameters
Input: G: Initial 3DGS from satellite-view training
Output: G': Refined 3DGS

$G' \leftarrow G$
for i = 1 to N_e **do**
  `radius` $\leftarrow R_i$
  `elevation` $\leftarrow E_i$
  `cam_views` $\leftarrow$ ORBITVIEWS($\{P\}$, `radius`, `elevation`, N_v) ▷ Generate $N_p \times N_v$ views
  `render_views` $\leftarrow$ RENDER(G', `cam_views`) ▷ Render RGB images
  `refine_views` $\leftarrow$ FLOWEDITREFINE(`render_views`, $T_{\text{src}}, T_{\text{tgt}}, n_{\min}, n_{\max}, N_s$) ▷ Refine renders using FlowEdit
  $G' \leftarrow$ TRAIN(G', `refine_views`) ▷ Update 3DGS using refined views
end for
return G'

Optimization. For each episode i, we optimize the 3DGS using:

$$\mathcal{L}_{\text{IDU}}(G_{i-1}, \tilde{C}_i) = \mathcal{L}_{\text{color}} + \lambda_{\text{depth}} \mathcal{L}_{\text{depth}} \ , \tag{5}$$

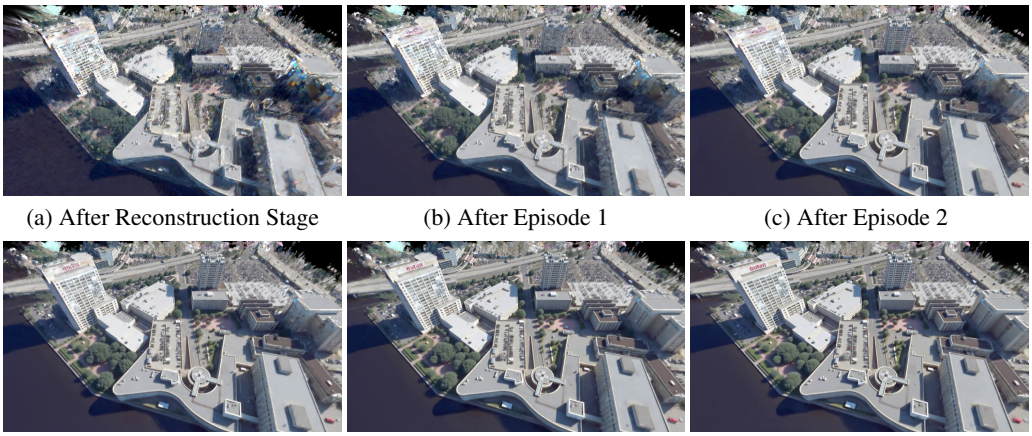

(a) After Reconstruction Stage (b) After Episode 1 (c) After Episode 2

(d) After Episode 3 (e) After Episode 4 (f) After Episode 5 (Final)

Figure 6: **Visualization of progressive refinement.** This figure illustrates the step-by-step evolution of the synthesized 3D scene. Starting from the initial reconstruction state (a), the geometry and texture are progressively refined through successive stages of the iterative process (b-e), culminating in the final high-fidelity result (f).

where G_{i-1} denotes the previous episode's 3DGS model, and $\tilde{C}_i$ are the current refined images. We provide more implementation details in Section A.1.

4 Experiments

Datasets. We evaluate on high-resolution RGB satellite imagery from two sources. First, the 2019 IEEE GRSS Data Fusion Contest (DFC2019) (Le Saux et al., 2019) featuring WorldView-3 captures of Jacksonville, Florida (2048×2048 pixels, 35 cm/pixel resolution). Camera parameters and sparse points were generated using SatelliteSfM (Zhang et al., 2019). We evaluate on four standard AOIs: JAX_004, JAX_068, JAX_214, and JAX_260, following Sat-NeRF (Marí et al., 2022) and EOGS (Savant Aira et al., 2025) protocols. Second, for geographic diversity, we use the GoogleEarth dataset (Xie et al., 2024) (training data for CityDreamer (Xie et al., 2024) and GaussianCity (Xie et al., 2025b)) containing NYC scenes. We use four scenes (004, 010, 219, 336) with training views rendered at an 80° elevation to approximate satellite conditions. Google Earth Studio (GES) (Google, 2024) renders serve as ground truth for both datasets. See Section A.2 for more detail about datasets.

Baselines. Our method connects satellite-based 3D reconstruction and city generation, requiring baselines from both fields. For *satellite reconstruction*, we compare with Sat-NeRF (Marí et al., 2022) and EOGS (Savant Aira et al., 2025) on DFC2019 (they require RPC input unavailable in GoogleEarth), plus Mip-Splatting (Yu et al., 2024) (enhanced with our appearance modeling) and CoR-GS Zhang et al. (2024b) on both datasets.[1] For *city generation*, we compare with CityDreamer (Xie et al., 2024) and GaussianCity (Xie et al., 2025b) on GoogleEarth (their training dataset). We use official implementations with default settings. All experiments run on a single RTX A6000 GPU.

Evaluation metrics. We primarily use distribution-based metrics to quantify quality and diversity. We report FID_{CLIP} (Kynkäänniemi et al., 2023) and CMMD (Jayasumana et al., 2024) that use the CLIP (Radford et al., 2021) backbone. This is based on their observations that the InceptionV3 (Szegedy et al., 2016) used in the classic FID (Heusel et al., 2017) and KID (Binkowski et al., 2018) is unsuitable for modern generative models. We complement these with user studies for perceptual quality assessment. We also report pixel-aligned metrics (PSNR (Huynh-Thu & Ghanbari, 2008), SSIM (Wang et al., 2004), LPIPS (Zhang et al., 2018)) as secondary references. While generally unsuitable for generative tasks, these metrics are meaningful for the Google Earth dataset, where all images come from the same consistent GES 3D representation, eliminating temporal variations.

[1]Many methods lack available code or models: Sat2Scene (Li et al., 2024d), Sat2Vid (Li et al., 2021), EO-NeRF (Marí et al., 2023), Sat-DN (Liu et al., 2025b), SatelliteRF (Zhou et al., 2024b), Sat-Mesh (Qu & Deng, 2023), CrossViewDiff (Li et al., 2024c), SkySplat (Huang et al., 2025), and others.

Table 1: **Quantitative comparison of different methods on DFC2019 (Le Saux et al., 2019)**. The results show that our method consistently achieves the best performance, indicating superior perceptual fidelity compared to all baselines. Metrics are computed between renders from each method and reference frames from GES.

Methods	Distribution Metrics		Pixel-level Metrics*		
	FID_{CLIP} ↓	CMMD ↓	PSNR ↑	SSIM ↑	LPIPS ↓
3D Reconstruction					
Sat-NeRF (Marí et al., 2022)	88.36	4.868	10.05	0.269	0.864
EOGS (Savant Aira et al., 2025)	87.74	5.286	7.26	0.168	0.959
Mip-Splatting (Yu et al., 2024)	87.19	5.405	11.89	0.318	0.819
CoR-GS (Zhang et al., 2024b)	89.03	5.241	11.55	**0.350**	0.948
Our Approach					
Ours	**27.35**	**2.086**	**12.38**	0.321	**0.791**

Table 2: **Quantitative comparison of different methods on GoogleEarth dataset (Xie et al., 2024).** The results show that our approach consistently achieves the best performance, indicating superior perceptual fidelity compared to all baselines. Metrics are computed between renders from each method and reference frames from GES.

Methods	Distribution Metrics		Pixel-level Metrics		
	FID_{CLIP} ↓	CMMD ↓	PSNR ↑	SSIM ↑	LPIPS ↓
City Generation					
CityDreamer (Xie et al., 2024)	36.52	4.152	12.58	0.267	0.558
GaussianCity (Xie et al., 2025b)	28.73	2.917	13.41	0.291	0.541
3D Reconstruction					
CoR-GS (Zhang et al., 2024b)	27.32	3.752	12.85	0.291	0.455
Our Approach					
Ours	**9.91**	**2.009**	**14.28**	**0.298**	**0.394**

4.1 Comparisons with Baselines

Quantitative comparison. We evaluate against both satellite reconstruction and city generation methods using distribution-based metrics. Evaluation images are created by dividing rendered frames into 144 patches (512×512 pixels). For comparison in the DFC2019 dataset, we render GES reference videos at 17° elevation, extracting 30 frames per AOI (4,320 images total). For comparison in the GoogleEarth dataset, we use 45° elevation with 24 frames per scene (3,456 images total). We generate matching videos from all methods using identical camera parameters. Our method consistently outperforms all baselines across all metrics on both the DFC2019 and Google Earth datasets (Tables 1 and 2), demonstrating effective reconstruction across diverse urban environments.

Qualitative comparison. Figure 7(a) presents comparisons on the DFC2019 dataset against Sat-NeRF (Marí et al., 2022), EOGS (Savant Aira et al., 2025), and Mip-Splatting (Yu et al., 2024). All baselines exhibit significant distortions and blurry textures at lower viewpoints, while our baseline without IDU improves geometry but still shows floating artifacts and lacks facade detail. Our full approach achieves superior image quality. Figure 7(b) compares our approach on the GoogleEarth dataset against CityDreamer (Xie et al., 2024), GaussianCity (Xie et al., 2025b), and CoR-GS (Zhang et al., 2024b). While CityDreamer and GaussianCity generate plausible scenes, they produce oversimplified geometry and inaccurate textures, missing distinctive features such as the red pavement in scene 010 that our method correctly synthesizes. In contrast, our complete method achieves sharper building contours, enhanced texture fidelity, and reduced artifacts across both comparison scenarios. Notably, our approach successfully synthesizes plausible details for building facades occluded in the input satellite imagery and accurately reconstructs complex features including vegetation and multi-level architectures with finer surface details that better match the reference images. The visual quality approaches GES reference renders despite using only satellite imagery without ground-level data. Additional qualitative results are presented in Section A.2.

User studies. We conducted two comparative evaluations with 89 participants each: first, participants assessed the satellite input, GES reference video, Sat-NeRF, EOGS, CoR-GS, and our approach; second, participants compared the satellite input, GES reference video, CityDreamer, GaussianCity, CoR-GS, and our approach. Both studies evaluated geometric accuracy, spatial alignment, and overall quality, with full survey details in Section A.2. On the DFC2019 dataset, our method achieved dominant winrates of ≈97%/97%/97% vs. Sat-NeRF's ≈3%/3%/3%, while EOGS and CoR-GS achieved 0%/0%/0%. On the GoogleEarth dataset, our approach maintained a clear advantage with ≈90%/90%/92% winrates vs. CityDreamer's ≈4%/3%/3%, GaussianCity's ≈3%/3%/3%, and CoR-GS's ≈3%/4%/2%. These results consistently validate that our approach significantly outperforms all baselines under human perception across geometric accuracy, spatial alignment, and overall quality.

Rendering efficiency. Our method achieves 11 FPS on the modest NVIDIA T4 GPU, significantly outperforming CityDreamer's 0.18 FPS despite running on the far more powerful NVIDIA A100, which offers 5× the CUDA cores and 10× the memory bandwidth. GaussianCity reaches comparable speeds (10.72 FPS) but requires the high-end A100. Furthermore, our fused representation enables real-time rendering at 40 FPS on consumer hardware (MacBook Air M2), demonstrating that our method enables high-quality 3D urban navigation without specialized computing resources.

4.2 Ablation Studies

We conduct ablation studies on the JAX_068 AOI.

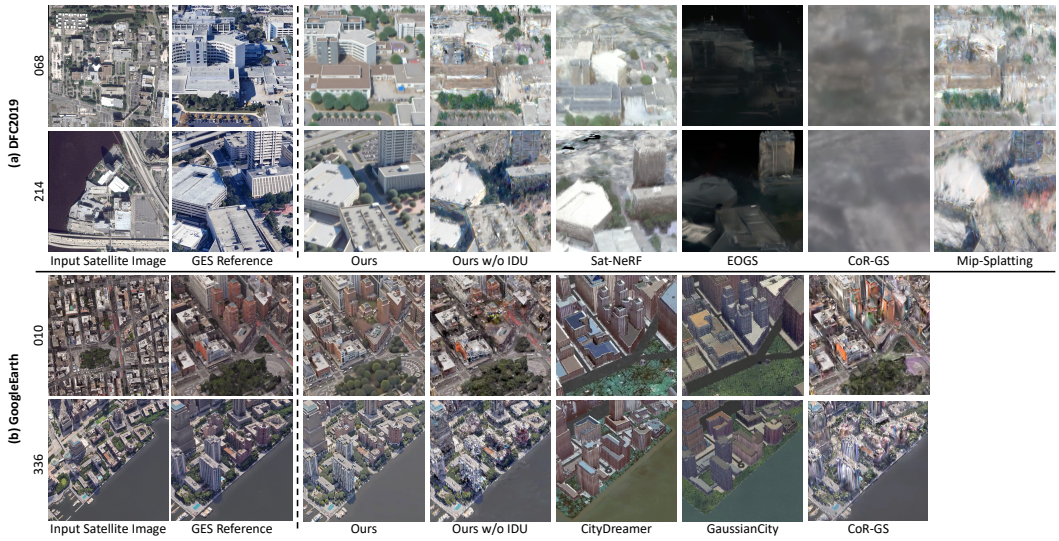

Figure 7: **Qualitative comparison on (a) DFC2019 and (b) GoogleEarth datasets.** The leftmost column shows one representative example of the input satellite images. Our method outperforms all baselines in geometric accuracy and texture quality in low-altitude novel views, demonstrating enhanced building geometry, detailed facades, and reduced floating artifacts. Notably, our approach correctly preserves distinctive features such as the red pavement in scene 010 that competing methods miss. Unlike CityDreamer (Xie et al., 2024) and GaussianCity (Xie et al., 2025b), our method operates directly on satellite imagery without requiring pixel-aligned semantic maps or height-fields, enabling synthesis of complex geometric structures that more closely match GES references.

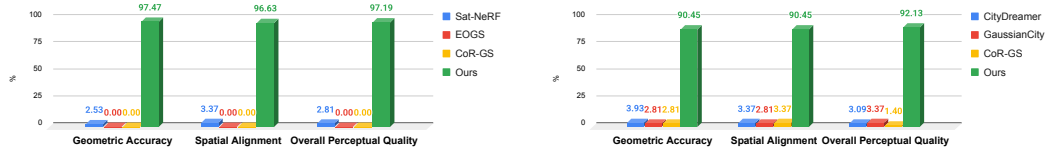

(a) Compare on DFC2019 dataset. (b) Compare on GoogleEarth dataset.

Figure 8: **User study results.** Our method consistently outperforms Sat-NeRF (Marí et al., 2022), EOGS (Savant Aira et al., 2025), CoR-GS (Zhang et al., 2024b), CityDreamer (Xie et al., 2024) and GaussianCity (Xie et al., 2025b), achieving particularly high scores in geometric accuracy and overall perceptual quality. (a) details the comparison on the DFC2019 dataset (Le Saux et al., 2019), while subfigure (b) details the comparison on the GoogleEarth dataset (Xie et al., 2024).

Ablation on the reconstruction stage. We ablate appearance modeling, opacity regularization, and pseudo-camera depth supervision (see Table 3 and Figure 9). For this ablation, we evaluate at higher elevation angles to assess the quality of renders during the IDU process, rather than testing the final low-angle performance. Appearance modeling is crucial for multi-date convergence, opacity regularization removes floating artifacts (Figure 9(a)), and depth supervision flattens planar regions (Figure 9(b)). Together, they yield the lowest FID_{CLIP}/CMMD scores. Furthermore, we validate geometric accuracy using LiDAR data from the DFC2019 dataset (Le Saux et al., 2019). To quantify this, we unproject 3DGS depth renders into point clouds and rasterize them into Digital Surface Models (DSMs) for comparison. Our results show that both opacity regularization and pseudo-depth supervision improve geometric accuracy, with their combination achieving the lowest MAE/RMSE.

Ablation on the synthesis stage. We isolate two key factors: multi-sample diffusion and curriculum view progression. As Figure 9(c) shows, $N_s = 2$ achieves the optimal visual results. Although $N_s = 5$ yields the lowest CMMD, it requires a $1.5\times$ increase in training time with marginal returns in quality; thus, we adopt $N_s = 2$ for all experiments. Additionally, Figure 9(d) highlights that employing a curriculum strategy (vs. random views) effectively restores geometry in occluded areas, a benefit confirmed by Table 4. We further benchmark our refinement module against the SDEdit (Meng et al., 2022) baseline. As evident in Figure 9(e), SDEdit causes significant degradation, primarily due to its inability to hallucinate details while maintaining the structural integrity defined by the satellite imagery. Finally, we evaluate prompt sensitivity by utilizing generic context-free prompts. The negligible visual difference in Figure 9(e) confirms that our method is robust to prompt

Table 3: **Ablation on the reconstruction stage.** Appearance modeling secures convergence. Opacity regularization and depth supervision enhance visual fidelity and geometric accuracy.

Components			Perceptual Metrics		Geometric Metrics	
App. Mod.	Op. Reg.	Depth Sup.	FID_{CLIP} ↓	CMMD ↓	MAE (m)↓	RMSE (m)↓
✗	✗	✗	*Failed*	*Failed*	*Failed*	*Failed*
✓	✗	✗	41.90	2.45	3.542	5.218
✓	✓	✗	39.95	2.40	2.980	4.527
✓	✓	✓	**38.01**	**2.31**	**2.250**	**3.483**

Table 4: **Ablation on the synthesis stage.** We evaluate sample counts (N_s), core components, and compare against baselines.

Method Variation	FID_{CLIP} ↓	CMMD ↓	Time (h)
Multiple Samples (N_s)			
$N_s = 1$	34.11	3.19	3.44
Ours ($N_s = 2$)	**28.35**	2.88	6.37
$N_s = 3$	28.64	2.77	7.19
$N_s = 5$	29.17	**2.68**	9.80
Component Ablation			
w/o Curriculum	33.79	3.36	-
w/ Context-free Pmt.	30.78	2.98	-
Replaced w/ SDEdit	64.74	4.14	-

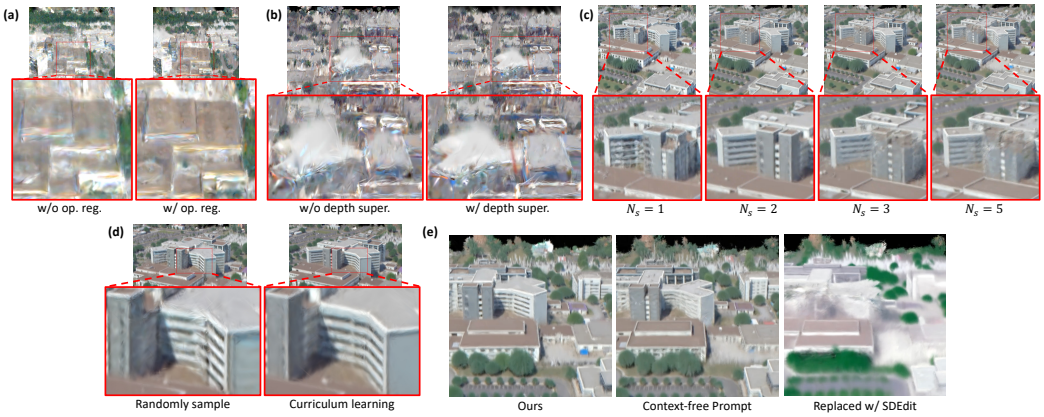

Figure 9: **Satellite-view training and IDU refinement ablation.** (a) Opacity regularization reduces floating artifacts and yields denser reconstructions. (b) Pseudo-camera depth supervision improves geometry in planar, texture-less areas like rooftops and roads. (c) Using multiple diffusion samples per view enhances texture consistency and reduces high-frequency geometric noise, $N_s = 2$ achieves the optimal visual results. (d) Curriculum learning progressively introduces challenging views, significantly improving geometric coherence in previously occluded regions compared to random sampling. (e) Refinement analysis: Using a generic context-free prompt results in a minor degradation of facade details but maintains structure, demonstrating robustness. In contrast, replacing our refinement method with SDEdit leads to a severe drop in quality, as standard noising-denoising struggles to hallucinate details while preserving the underlying geometry defined by the satellite imagery.

engineering and driven primarily by the diffusion model's internal priors. Please refer to Table 10 for the specific text prompts.

5 Conclusion

Skyfall-GS synthesizes real-time, immersive 3D urban scenes from multi-view satellite imagery, using 3D Gaussian Splatting and text-to-image diffusion models in a curriculum-based iterative refinement approach. Our method surpasses existing methods like Sat-NeRF, , EOGS, CityDreamer, and GaussianCity, effectively addressing challenges such as limited parallax, illumination variations, and occlusions. Future work includes scaling to larger environments and dynamic scenes.

Limitations. Our method requires significant computational resources, primarily due to the refinement process. The fixed heuristic camera trajectory creates blind spots in complex urban geometries, particularly in heavily occluded regions and scene boundaries. This results in artifacts and over-smoothed textures at extreme street-level perspectives. Additionally, our hybrid reconstruction-generation framework requires off-nadir satellite views. It cannot synthesize facades from purely top-down (nadir) imagery.

Ethics Statement

This work included a small-scale user study where anonymous participants were asked to compare our results with baselines through an online survey. No personally identifiable information was collected, and all responses were stored anonymously. Participation was entirely voluntary, and no risks were posed to participants. The study did not require institutional review board (IRB) approval under our institution's policies, as it involved only anonymous survey responses with minimal risk.

Reproducibility Statement

We have taken several steps to ensure the reproducibility of our work. Implementation details of our reconstruction and synthesis pipeline are provided in Section 3, including the architecture, loss functions, and optimization objectives. All hyperparameters, training schedules, and regularization terms are described in Section 3 and Section A.1. Details of datasets, splits, and evaluation protocols are described in Section 4 and Section A.2, with clear references to the publicly available DFC2019 dataset and GoogleEarth dataset. Details of the user study are described in Section A.2. We will release our source code upon acceptance to further support transparency and reproducibility.

References

Jonathan T. Barron, Ben Mildenhall, Matthew Tancik, Peter Hedman, Ricardo Martin-Brualla, and Pratul P. Srinivasan. Mip-NeRF: A multiscale representation for anti-aliasing neural radiance fields, 2021.

Jonathan T. Barron, Ben Mildenhall, Dor Verbin, Pratul P. Srinivasan, and Peter Hedman. Mip-NeRF 360: Unbounded anti-aliased neural radiance fields. *CVPR*, 2022.

Jonathan T. Barron, Ben Mildenhall, Dor Verbin, Pratul P. Srinivasan, and Peter Hedman. Zip-NeRF: Anti-aliased grid-based neural radiance fields. In *ICCV*, 2023.

Mikołaj Binkowski, Dougal J Sutherland, Michael Arbel, and Arthur Gretton. Demystifying MMD GANs. In *International Conference on Learning Representations*, 2018.

Marc Bosch, Zachary Kurtz, Shea Hagstrom, and Myron Brown. A multiple view stereo benchmark for satellite imagery. In *2016 IEEE Applied Imagery Pattern Recognition Workshop (AIPR)*, pp. 1–9. IEEE, 2016.

Tim Brooks, Aleksander Holynski, and Alexei A Efros. InstructPix2Pix: Learning to follow image editing instructions. In *Proceedings of the IEEE/CVF Conference on Computer Vision and Pattern Recognition*, pp. 18392–18402, 2023.

Hao Chen, Jiafu Wu, Ying Jin, Jinlong Peng, Xiaofeng Mao, Mingmin Chi, Mufeng Yao, Bo Peng, Jian Li, and Yun Cao. VI3DRM: Towards meticulous 3D reconstruction from sparse views via photo-realistic novel view synthesis, 2024. URL https://arxiv.org/abs/2409.08207.

Jaeyoung Chung, Suyoung Lee, Hyeongjin Nam, Jaerin Lee, and Kyoung Mu Lee. LucidDreamer: Domain-free generation of 3D gaussian splatting scenes. *arXiv preprint arXiv:2311.13384*, 2023.

Hiba Dahmani, Moussab Bennehar, Nathan Piasco, Luis Roldao, and Dzmitry Tsishkou. SWAG: Splatting in the wild images with appearance-conditioned gaussians, 2024. URL https://arxiv.org/abs/2403.10427.

Boyang Deng, Richard Tucker, Zhengqi Li, Leonidas Guibas, Noah Snavely, and Gordon Wetzstein. Streetscapes: Large-scale consistent street view generation using autoregressive video diffusion. In *SIGGRAPH 2024 Conference Papers*, 2024.

Dawa Derksen and Dario Izzo. Shadow neural radiance fields for multi-view satellite photogrammetry. In *Proceedings of the IEEE/CVF Conference on Computer Vision and Pattern Recognition (CVPR) Workshops*, pp. 1152–1161, June 2021.

Jan-Niklas Dihlmann, Andreas Engelhardt, and Hendrik P.A. Lensch. SIGNeRF: Scene integrated generation for neural radiance fields. In *Proceedings of the IEEE/CVF Conference on Computer Vision and Pattern Recognition (CVPR)*, 2024.

Cheng-De Fan, Chen-Wei Chang, Yi-Ruei Liu, Jie-Ying Lee, Jiun-Long Huang, Yu-Chee Tseng, and Yu-Lun Liu. Spectromotion: Dynamic 3d reconstruction of specular scenes. In *Proceedings of the Computer Vision and Pattern Recognition Conference*, pp. 21328–21338, 2025.

Zhiwen Fan, Wenyan Cong, Kairun Wen, Kevin Wang, Jian Zhang, Xinghao Ding, Danfei Xu, Boris Ivanovic, Marco Pavone, Georgios Pavlakos, et al. InstantSplat: Unbounded sparse-view pose-free gaussian splatting in 40 seconds. *arXiv preprint arXiv:2403.20309*, 2(3):4, 2024.

Jiemin Fang, Junjie Wang, Xiaopeng Zhang, Lingxi Xie, and Qi Tian. GaussianEditor: Editing 3D gaussians delicately with text instructions. In *CVPR*, 2024.

Jian Gao, Jin Liu, and Shunping Ji. Rational polynomial camera model warping for deep learning based satellite multi-view stereo matching. In *Proceedings of the IEEE/CVF international conference on computer vision*, pp. 6148–6157, 2021.

Jian Gao, Jin Liu, and Shunping Ji. A general deep learning based framework for 3D reconstruction from multi-view stereo satellite images. *ISPRS Journal of Photogrammetry and Remote Sensing*, 195:446–461, 2023a. ISSN 0924-2716. doi: https://doi.org/10.1016/j.isprsjprs.2022.12.012. URL https://www.sciencedirect.com/science/article/pii/S0924271622003276.

Jian Gao, Jin Liu, and Shunping Ji. A general deep learning based framework for 3d reconstruction from multi-view stereo satellite images. *ISPRS Journal of Photogrammetry and Remote Sensing*, 195:446–461, 2023b.

Kyle Gao, Dening Lu, Hongjie He, Linlin Xu, and Jonathan Li. Enhanced 3D urban scene reconstruction and point cloud densification using gaussian splatting and google earth imagery, 2024a. URL https://arxiv.org/abs/2405.11021.

Ruiqi Gao, Aleksander Holynski, Philipp Henzler, Arthur Brussee, Ricardo Martin-Brualla, Pratul P. Srinivasan, Jonathan T. Barron, and Ben Poole. CAT3D: Create anything in 3D with multi-view diffusion models. *Advances in Neural Information Processing Systems*, 2024b.

Ruiyuan Gao, Kai Chen, Enze Xie, Lanqing Hong, Zhenguo Li, Dit-Yan Yeung, and Qiang Xu. Magicdrive: Street view generation with diverse 3d geometry control. *arXiv preprint arXiv:2310.02601*, 2023c.

Google. Google earth studio. https://earth.google.com/studio, 2024. Accessed: 2025-05-14.

Ayaan Haque, Matthew Tancik, Alexei Efros, Aleksander Holynski, and Angjoo Kanazawa. Instruct-NeRF2NeRF: Editing 3D scenes with instructions. In *Proceedings of the IEEE/CVF International Conference on Computer Vision*, 2023.

Amir Hertz, Ron Mokady, Jay Tenenbaum, Kfir Aberman, Yael Pritch, and Daniel Cohen-Or. Prompt-to-prompt image editing with cross attention control. *arXiv preprint arXiv:2208.01626*, 2022.

Martin Heusel, Hubert Ramsauer, Thomas Unterthiner, Bernhard Nessler, and Sepp Hochreiter. GANs trained by a two time-scale update rule converge to a local nash equilibrium. In *Advances in Neural Information Processing Systems*, pp. 6626–6637, 2017.

Hao-Yu Hou, Chia-Chi Hsu, Yu-Chen Huang, Mu-Yi Shen, Wei-Fang Sun, Cheng Sun, Chia-Che Chang, Yu-Lun Liu, and Chun-Yi Lee. 3d gaussian splatting with grouped uncertainty for unconstrained images. In *ICASSP 2025-2025 IEEE International Conference on Acoustics, Speech and Signal Processing (ICASSP)*, pp. 1–5. IEEE, 2025.

Xuejun Huang, Xinyi Liu, Yi Wan, Zhi Zheng, Bin Zhang, Mingtao Xiong, Yingying Pei, and Yongjun Zhang. SkySplat: Generalizable 3d gaussian splatting from multi-temporal sparse satellite images. *arXiv preprint arXiv:2508.09479*, 2025.

Quan Huynh-Thu and Mohammed Ghanbari. Scope of validity of PSNR in image/video quality assessment. *Electronics Letters*, 44(13):800–801, 2008.

Sadeep Jayasumana, Srikumar Ramalingam, Andreas Veit, Daniel Glasner, Ayan Chakrabarti, and Sanjiv Kumar. Rethinking FID: Towards a better evaluation metric for image generation. In *CVPR*, 2024.

Bernhard Kerbl, Georgios Kopanas, Thomas Leimkühler, and George Drettakis. 3D gaussian splatting for real-time radiance field rendering. *ACM TOG*, 2023.

Bernhard Kerbl, Andreas Meuleman, Georgios Kopanas, Michael Wimmer, Alexandre Lanvin, and George Drettakis. A hierarchical 3D gaussian representation for real-time rendering of very large datasets. *ACM TOG*, 2024.

Jonas Kulhanek, Songyou Peng, Zuzana Kukelova, Marc Pollefeys, and Torsten Sattler. WildGaussians: 3D gaussian splatting in the wild. *NeurIPS*, 2024.

Vladimir Kulikov, Matan Kleiner, Inbar Huberman-Spiegelglas, and Tomer Michaeli. FlowEdit: Inversion-free text-based editing using pre-trained flow models. *arXiv preprint arXiv:2412.08629*, 2024.

Tuomas Kynkäänniemi, Tero Karras, Miika Aittala, Timo Aila, and Jaakko Lehtinen. The role of ImageNet classes in fréchet inception distance. In *Proc. ICLR*, 2023.

Black Forest Labs. Official weights of FLUX.1 dev. `https://huggingface.co/black-forest-labs/FLUX.1-dev`, 2024a. Accessed: 2025-02-28.

Black Forest Labs. FLUX. `https://github.com/black-forest-labs/flux`, 2024b. Accessed: 2025-02-28.

Bertrand Le Saux, Naoto Yokoya, Ronny Hänsch, and Myron Brown. Data fusion contest 2019 (DFC2019), 2019. URL `https://dx.doi.org/10.21227/c6tm-vw12`.

Matthew J. Leotta, Chengjiang Long, Bastien Jacquet, Matthieu Zins, Dan Lipsa, Jie Shan, Bo Xu, Zhixin Li, Xu Zhang, Shih-Fu Chang, Matthew Purri, Jia Xue, and Kristin Dana. Urban semantic 3D reconstruction from multiview satellite imagery. In *Proceedings of the IEEE/CVF Conference on Computer Vision and Pattern Recognition (CVPR) Workshops*, June 2019.

Haoran Li, Haolin Shi, Wenli Zhang, Wenjun Wu, Yong Liao, Lin Wang, Lik-hang Lee, and Peng Yuan Zhou. DreamScene: 3D gaussian-based text-to-3D scene generation via formation pattern sampling. In *European Conference on Computer Vision*, pp. 214–230. Springer, 2024a.

Jiahe Li, Jiawei Zhang, Xiao Bai, Jin Zheng, Xin Ning, Jun Zhou, and Lin Gu. DNGaussian: Optimizing sparse-view 3D gaussian radiance fields with global-local depth normalization. *arXiv preprint arXiv:2403.06912*, 2024b.

Weijia Li, Jun He, Junyan Ye, Huaping Zhong, Zhimeng Zheng, Zilong Huang, Dahua Lin, and Conghui He. CrossViewDiff: A cross-view diffusion model for satellite-to-street view synthesis, 2024c. URL `https://arxiv.org/abs/2408.14765`.

Z Li, W Wang, H Li, E Xie, C Sima, T Lu, Q Yu, and J Dai. Bevformer: Learning bird's-eye-view representation from multi-camera images via spatiotemporal transformers. arxiv 2022. In *ECCV*, 2022.

Zuoyue Li, Zhenqiang Li, Zhaopeng Cui, Rongjun Qin, Marc Pollefeys, and Martin R. Oswald. Sat2Vid: Street-view panoramic video synthesis from a single satellite image, 2021. URL `https://arxiv.org/abs/2012.06628`.

Zuoyue Li, Zhenqiang Li, Zhaopeng Cui, Marc Pollefeys, and Martin R. Oswald. Sat2Scene: 3D urban scene generation from satellite images with diffusion. In *Proceedings of the IEEE/CVF Conference on Computer Vision and Pattern Recognition (CVPR)*, pp. 7141–7150, June 2024d.

Chen-Hsuan Lin, Jun Gao, Luming Tang, Towaki Takikawa, Xiaohui Zeng, Xun Huang, Karsten Kreis, Sanja Fidler, Ming-Yu Liu, and Tsung-Yi Lin. Magic3D: High-resolution text-to-3D content creation. In *CVPR*, 2023a.

Chieh Hubert Lin, Hsin-Ying Lee, Willi Menapace, Menglei Chai, Aliaksandr Siarohin, Ming-Hsuan Yang, and Sergey Tulyakov. InfiniCity: Infinite-scale city synthesis. In *Proceedings of the IEEE/CVF International Conference on Computer Vision*, 2023b.

Chin-Yang Lin, Chung-Ho Wu, Chang-Han Yeh, Shih-Han Yen, Cheng Sun, and Yu-Lun Liu. Frugalnerf: Fast convergence for extreme few-shot novel view synthesis without learned priors. In *Proceedings of the Computer Vision and Pattern Recognition Conference*, pp. 11227–11238, 2025.

Jiaqi Lin, Zhihao Li, Xiao Tang, Jianzhuang Liu, Shiyong Liu, Jiayue Liu, Yangdi Lu, Xiaofei Wu, Songcen Xu, Youliang Yan, and Wenming Yang. VastGaussian: Vast 3D gaussians for large scene reconstruction, 2024. URL https://arxiv.org/abs/2402.17427.

Kuan-Hung Liu, Cheng-Kun Yang, Min-Hung Chen, Yu-Lun Liu, and Yen-Yu Lin. Corrfill: Enhancing faithfulness in reference-based inpainting with correspondence guidance in diffusion models. In *2025 IEEE/CVF Winter Conference on Applications of Computer Vision (WACV)*, pp. 1618–1627. IEEE, 2025a.

Ruoshi Liu, Rundi Wu, Basile Van Hoorick, Pavel Tokmakov, Sergey Zakharov, and Carl Vondrick. Zero-1-to-3: Zero-shot one image to 3D object. In *CVPR*, 2023a.

Tianle Liu, Shuangming Zhao, Wanshou Jiang, and Bingxuan Guo. Sat-DN: Implicit surface reconstruction from multi-view satellite images with depth and normal supervision, 2025b. URL https://arxiv.org/abs/2502.08352.

Xinhang Liu, Jiaben Chen, Shiu-hong Kao, Yu-Wing Tai, and Chi-Keung Tang. Deceptive-NeRF/3DGS: Diffusion-generated pseudo-observations for high-quality sparse-view reconstruction. *arXiv preprint arXiv:2305.15171*, 2023b.

Yang Liu, Chuanchen Luo, Zhongkai Mao, Junran Peng, and Zhaoxiang Zhang. CityGaussianV2: Efficient and geometrically accurate reconstruction for large-scale scenes, 2024. URL https://arxiv.org/abs/2411.00771.

Yang Liu, Chuanchen Luo, Lue Fan, Naiyan Wang, Junran Peng, and Zhaoxiang Zhang. CityGaussian: Real-time high-quality large-scale scene rendering with gaussians. In *European Conference on Computer Vision*, pp. 265–282. Springer, 2025c.

Roger Marí, Gabriele Facciolo, and Thibaud Ehret. Sat-NeRF: Learning multi-view satellite photogrammetry with transient objects and shadow modeling using RPC cameras. In *2022 IEEE/CVF Conference on Computer Vision and Pattern Recognition Workshops (CVPRW)*, pp. 1310–1320, 2022.

Roger Marí, Gabriele Facciolo, and Thibaud Ehret. Multi-date earth observation NeRF: The detail is in the shadows. In *Proceedings of the IEEE/CVF Conference on Computer Vision and Pattern Recognition (CVPR) Workshops*, pp. 2034–2044, June 2023.

Ricardo Martin-Brualla, Noha Radwan, Mehdi SM Sajjadi, Jonathan T Barron, Alexey Dosovitskiy, and Daniel Duckworth. NeRF in the wild: Neural radiance fields for unconstrained photo collections. In *CVPR*, 2021.

Luke Melas-Kyriazi, Iro Laina, Christian Rupprecht, Natalia Neverova, Andrea Vedaldi, Oran Gafni, and Filippos Kokkinos. IM-3D: Iterative multiview diffusion and reconstruction for high-quality 3D generation. *International Conference on Machine Learning*, 2024.

Chenlin Meng, Yutong He, Yang Song, Jiaming Song, Jiajun Wu, Jun-Yan Zhu, and Stefano Ermon. SDEdit: Guided image synthesis and editing with stochastic differential equations. In *International Conference on Learning Representations*, 2022.

Ben Mildenhall, Pratul P Srinivasan, Matthew Tancik, Jonathan T Barron, Ravi Ramamoorthi, and Ren Ng. NeRF: Representing scenes as neural radiance fields for view synthesis. *Communications of the ACM*, 2021.

Ashkan Mirzaei, Tristan Aumentado-Armstrong, Konstantinos G Derpanis, Jonathan Kelly, Marcus A Brubaker, Igor Gilitschenski, and Alex Levinshtein. Spin-NeRF: Multiview segmentation and perceptual inpainting with neural radiance fields. In *Proceedings of the IEEE/CVF Conference on Computer Vision and Pattern Recognition*, pp. 20669–20679, 2023.

Ashkan Mirzaei, Tristan Aumentado-Armstrong, Marcus A. Brubaker, Jonathan Kelly, Alex Levinshtein, Konstantinos G. Derpanis, and Igor Gilitschenski. Watch your steps: Local image and scene editing by text instructions. In *ECCV*, 2024.

Daiki Miyake, Akihiro Iohara, Yu Saito, and Toshiyuki Tanaka. Negative-prompt inversion: Fast image inversion for editing with text-guided diffusion models, 2024. URL https://arxiv.org/abs/2305.16807.

Ron Mokady, Amir Hertz, Kfir Aberman, Yael Pritch, and Daniel Cohen-Or. Null-text inversion for editing real images using guided diffusion models. *arXiv preprint arXiv:2211.09794*, 2022.

Thomas Müller, Alex Evans, Christoph Schied, and Alexander Keller. Instant neural graphics primitives with a multiresolution hash encoding. *ACM Trans. Graph.*, 41(4):102:1–102:15, July 2022. doi: 10.1145/3528223.3530127. URL https://doi.org/10.1145/3528223.3530127.

Michael Niemeyer, Jonathan T Barron, Ben Mildenhall, Mehdi SM Sajjadi, Andreas Geiger, and Noha Radwan. RegNeRF: Regularizing neural radiance fields for view synthesis from sparse inputs. In *CVPR*, 2022.

Ben Poole, Ajay Jain, Jonathan T Barron, and Ben Mildenhall. DreamFusion: Text-to-3D using 2D diffusion. *arXiv preprint arXiv:2209.14988*, 2022.

Ming Qian, Jincheng Xiong, Gui-Song Xia, and Nan Xue. Sat2Density: Faithful density learning from satellite-ground image pairs. In *ICCV*, 2023.

Yingjie Qu and Fei Deng. Sat-Mesh: Learning neural implicit surfaces for multi-view satellite reconstruction. *Remote Sensing*, 15(17), 2023. ISSN 2072-4292. doi: 10.3390/rs15174297. URL https://www.mdpi.com/2072-4292/15/17/4297.

Alec Radford, Jong Wook Kim, Chris Hallacy, Aditya Ramesh, Gabriel Goh, Sandhini Agarwal, Girish Sastry, Amanda Askell, Pamela Mishkin, Jack Clark, et al. Learning transferable visual models from natural language supervision. In *Proceedings of the 38th International Conference on Machine Learning*, pp. 8748–8763. PMLR, 2021.

Robin Rombach, Andreas Blattmann, Dominik Lorenz, Patrick Esser, and Björn Ommer. High-resolution image synthesis with latent diffusion models. In *Proceedings of the IEEE/CVF Conference on Computer Vision and Pattern Recognition (CVPR)*, pp. 10684–10695, June 2022.

Sara Sabour, Lily Goli, George Kopanas, Mark Matthews, Dmitry Lagun, Leonidas Guibas, Alec Jacobson, David J. Fleet, and Andrea Tagliasacchi. SpotLessSplats: Ignoring distractors in 3D gaussian splatting. *arXiv preprint arXiv:2406.20055*, 2024.

Luca Savant Aira, Gabriele Facciolo, and Thibaud Ehret. Gaussian splatting for efficient satellite image photogrammetry. In *Proceedings of the IEEE/CVF Conference on Computer Vision and Pattern Recognition*, 2025.

Johannes Lutz Schönberger and Jan-Michael Frahm. Structure-from-motion revisited. In *Conference on Computer Vision and Pattern Recognition (CVPR)*, 2016.

Yu Shang, Yuming Lin, Yu Zheng, Hangyu Fan, Jingtao Ding, Jie Feng, Jiansheng Chen, Li Tian, and Yong Li. UrbanWorld: An urban world model for 3D city generation. *arXiv preprint arXiv:2407.11965*, 2024. URL https://arxiv.org/abs/2407.11965.

Jianxiong Shen, Antonio Agudo, Francesc Moreno-Noguer, and Adria Ruiz. Conditional-flow NeRF: Accurate 3d modelling with reliable uncertainty quantification. In *European Conference on Computer Vision*, pp. 540–557. Springer, 2022.

Yichun Shi, Peng Wang, Jianglong Ye, Mai Long, Kejie Li, and Xiao Yang. MVDream: Multi-view diffusion for 3d generation. *arXiv preprint arXiv:2308.16512*, 2023.

Yujiao Shi, Dylan Campbell, Xin Yu, and Hongdong Li. Geometry-guided street-view panorama synthesis from satellite imagery. In *IEEE TPAMI*, 2022.

Michael Sprintson, Rama Chellappa, and Cheng Peng. FusionRF: High-fidelity satellite neural radiance fields from multispectral and panchromatic acquisitions. *arXiv preprint arXiv:2409.15132*, 2024.

Wenqiang Sun, Shuo Chen, Fangfu Liu, Zilong Chen, Yueqi Duan, Jun Zhang, and Yikai Wang. DimensionX: Create any 3D and 4D scenes from a single image with controllable video diffusion. *arXiv preprint arXiv:2411.04928*, 2024.

Christian Szegedy, Vincent Vanhoucke, Sergey Ioffe, Jon Shlens, and Zbigniew Wojna. Rethinking the inception architecture for computer vision. In *CVPR*, 2016.

Matthew Tancik, Vincent Casser, Xinchen Yan, Sabeek Pradhan, Ben Mildenhall, Pratul P Srinivasan, Jonathan T Barron, and Henrik Kretzschmar. Block-NeRF: Scalable large scene neural view synthesis. In *CVPR*, 2022.

Jiaxiang Tang, Jiawei Ren, Hang Zhou, Ziwei Liu, and Gang Zeng. DreamGaussian: Generative gaussian splatting for efficient 3d content creation. *arXiv preprint arXiv:2309.16653*, 2023.

Aysim Toker, Qunjie Zhou, Maxim Maximov, and Laura Leal-Taixe. Coming down to earth: Satellite-to-street view synthesis for geo-localization. In *Proceedings of the IEEE/CVF Conference on Computer Vision and Pattern Recognition (CVPR)*, pp. 6488–6497, June 2021.

Haithem Turki, Deva Ramanan, and Mahadev Satyanarayanan. Mega-NeRF: Scalable construction of large-scale NeRFs for virtual fly-throughs. In *CVPR*, 2022.

Ruicheng Wang, Sicheng Xu, Cassie Dai, Jianfeng Xiang, Yu Deng, Xin Tong, and Jiaolong Yang. MoGe: Unlocking accurate monocular geometry estimation for open-domain images with optimal training supervision, 2024a. URL https://arxiv.org/abs/2410.19115.

Yuxuan Wang, Xuanyu Yi, Zike Wu, Na Zhao, Long Chen, and Hanwang Zhang. View-consistent 3D editing with gaussian splatting, 2025. URL https://arxiv.org/abs/2403.11868.

Yuze Wang, Junyi Wang, and Yue Qi. WE-GS: An in-the-wild efficient 3D gaussian representation for unconstrained photo collections, 2024b. URL https://arxiv.org/abs/2406.02407.

Zhengyi Wang, Cheng Lu, Yikai Wang, Fan Bao, Chongxuan Li, Hang Su, and Jun Zhu. ProlificDreamer: High-fidelity and diverse text-to-3d generation with variational score distillation. *Advances in neural information processing systems*, 36:8406–8441, 2023.

Zhou Wang, Alan C Bovik, Hamid R Sheikh, and Eero P Simoncelli. Image quality assessment: From error visibility to structural similarity. *IEEE Transactions on Image Processing*, 13(4):600–612, 2004.

Ethan Weber, Aleksander Holynski, Varun Jampani, Saurabh Saxena, Noah Snavely, Abhishek Kar, and Angjoo Kanazawa. NeRFiller: Completing scenes via generative 3D inpainting. In *CVPR*, 2024.

Chung-Ho Wu, Yang-Jung Chen, Ying-Huan Chen, Jie-Ying Lee, Bo-Hsu Ke, Chun-Wei Tuan Mu, Yi-Chuan Huang, Chin-Yang Lin, Min-Hung Chen, Yen-Yu Lin, and Yu-Lun Liu. AuraFusion360: Augmented unseen region alignment for reference-based 360° unbounded scene inpainting, 2025. URL https://arxiv.org/abs/2502.05176.

Jing Wu, Jia-Wang Bian, Xinghui Li, Guangrun Wang, Ian Reid, Philip Torr, and Victor Prisacariu. GaussCtrl: Multi-view consistent text-driven 3D gaussian splatting editing. *ECCV*, 2024a.

Rundi Wu, Ben Mildenhall, Philipp Henzler, Keunhong Park, Ruiqi Gao, Daniel Watson, Pratul P. Srinivasan, Dor Verbin, Jonathan T. Barron, Ben Poole, and Aleksander Holynski. ReconFusion: 3D reconstruction with diffusion priors. *arXiv preprint arXiv:2312.02981*, 2023.

Rundi Wu, Ruiqi Gao, Ben Poole, Alex Trevithick, Changxi Zheng, Jonathan T. Barron, and Aleksander Holynski. CAT4D: Create anything in 4D with multi-view video diffusion models, 2024b. URL https://arxiv.org/abs/2411.18613.

Haozhe Xie, Zhaoxi Chen, Fangzhou Hong, and Ziwei Liu. CityDreamer: Compositional generative model of unbounded 3D cities. In *CVPR*, 2024.

Haozhe Xie, Zhaoxi Chen, Fangzhou Hong, and Ziwei Liu. CityDreamer4D: Compositional generative model of unbounded 4D cities. *arXiv preprint arXiv:2501.08983*, 2025a.

Haozhe Xie, Zhaoxi Chen, Fangzhou Hong, and Ziwei Liu. Generative gaussian splatting for unbounded 3D city generation. In *CVPR*, 2025b.

Zhexiao Xiong, Xin Xing, Scott Workman, Subash Khanal, and Nathan Jacobs. Mixed-view panorama synthesis using geospatially guided diffusion. *Transactions on Machine Learning Research*, 2024.

Jiacong Xu, Yiqun Mei, and Vishal M. Patel. Wild-GS: Real-time novel view synthesis from unconstrained photo collections, 2024. URL https://arxiv.org/abs/2406.10373.

Ningli Xu and Rongjun Qin. Geospecific view generation geometry-context aware high-resolution ground view inference from satellite views. In *European Conference on Computer Vision*, pp. 349–366. Springer, 2024.

Ningli Xu and Rongjun Qin. Satellite to GroundScape—large-scale consistent ground view generation from satellite views. *arXiv preprint arXiv:2504.15786*, 2025.

Junyan Ye, Jun He, Weijia Li, Zhutao Lv, Jinhua Yu, Haote Yang, and Conghui He. Skydiffusion: Street-to-satellite image synthesis with diffusion models and bev paradigm. *arXiv e-prints*, pp. arXiv–2408, 2024a.

Mingqiao Ye, Martin Danelljan, Fisher Yu, and Lei Ke. Gaussian grouping: Segment and edit anything in 3D scenes. In *ECCV*, 2024b.

Taoran Yi, Jiemin Fang, Junjie Wang, Guanjun Wu, Lingxi Xie, Xiaopeng Zhang, Wenyu Liu, Qi Tian, and Xinggang Wang. GaussianDreamer: Fast generation from text to 3d gaussians by bridging 2d and 3d diffusion models. In *Proceedings of the IEEE/CVF Conference on Computer Vision and Pattern Recognition*, pp. 6796–6807, 2024.

Zehao Yu, Anpei Chen, Binbin Huang, Torsten Sattler, and Andreas Geiger. Mip-Splatting: Alias-free 3D gaussian splatting. In *CVPR*, 2024.

Xianghui Ze, Zhenbo Song, Qiwei Wang, Jianfeng Lu, and Yujiao Shi. Controllable satellite-to-street-view synthesis with precise pose alignment and zero-shot environmental control, 2025. URL https://arxiv.org/abs/2502.03498.

Yu-Ting Zhan, Cheng-Yuan Ho, Hebi Yang, Yi-Hsin Chen, Jui Chiu Chiang, Yu-Lun Liu, and Wen-Hsiao Peng. Cat-3dgs: A context-adaptive triplane approach to rate-distortion-optimized 3dgs compression. *arXiv preprint arXiv:2503.00357*, 2025.

Dongbin Zhang, Chuming Wang, Weitao Wang, Peihao Li, Minghan Qin, and Haoqian Wang. Gaussian in the wild: 3D gaussian splatting for unconstrained image collections. *arXiv preprint arXiv:2403.15704*, 2024a.

Jiawei Zhang, Jiahe Li, Xiaohan Yu, Lei Huang, Lin Gu, Jin Zheng, and Xiao Bai. CoR-GS: Sparse-view 3d gaussian splatting via co-regularization. In *ECCV*, 2024b.

Kai Zhang, Jin Sun, and Noah Snavely. Leveraging vision reconstruction pipelines for satellite imagery. In *IEEE International Conference on Computer Vision Workshops*, 2019.

Lulin Zhang and Ewelina Rupnik. Sparsesat-NeRF: Dense depth supervised neural radiance fields for sparse satellite images. *arXiv preprint arXiv:2309.00277*, 2023.

Richard Zhang, Phillip Isola, Alexei A Efros, Eli Shechtman, and Oliver Wang. The unreasonable effectiveness of deep features as a perceptual metric. In *Proceedings of the IEEE Conference on Computer Vision and Pattern Recognition*, pp. 586–595, 2018.

Shougao Zhang, Mengqi Zhou, Yuxi Wang, Chuanchen Luo, Rongyu Wang, Yiwei Li, Zhaoxiang Zhang, and Junran Peng. CityX: Controllable procedural content generation for unbounded 3D cities, 2024c. URL https://arxiv.org/abs/2407.17572.

Mengqi Zhou, Yuxi Wang, Jun Hou, Shougao Zhang, Yiwei Li, Chuanchen Luo, Junran Peng, and Zhaoxiang Zhang. SceneX: Procedural controllable large-scale scene generation via large-language models, 2024a. URL https://arxiv.org/abs/2403.15698.

Xin Zhou, Yang Wang, Daoyu Lin, Zehao Cao, Biqing Li, and Junyi Liu. SatelliteRF: Accelerating 3D reconstruction in multi-view satellite images with efficient neural radiance fields. *Applied Sciences*, 14(7), 2024b. ISSN 2076-3417. doi: 10.3390/app14072729. URL https://www.mdpi.com/2076-3417/14/7/2729.

Zehao Zhu, Zhiwen Fan, Yifan Jiang, and Zhangyang Wang. FSGS: Real-time few-shot view synthesis using gaussian splatting, 2023.

A APPENDIX

This supplementary material provides additional details that complement our main paper. We include:

1. **Implementation Details**: This section details the pseudo-camera depth supervision strategy, 3DGS reconstruction parameters for satellite imagery, and the FlowEdit-based refinement process. We also provide a detailed breakdown of training time and memory consumption. Furthermore, we include a discussion on the validity of the RPC to perspective camera model approximation, including quantitative error analysis.
2. **Experiments Detail**: We provide dataset details, including training image counts and geographical coordinates for each Area of Interest (AOI), alongside the user study methodology and evaluation protocol.
3. **Additional Qualitative Results**: We present extended visual comparisons with state-of-the-art methods and results on four additional AOIs of the DFC2019 dataset. Furthermore, we provide visualizations of renders conditioned on varying per-image embeddings e_j to illustrate temporal stability.
4. **Additional Experiments & Results**: We encompass a comprehensive set of new experiments, including: (i) synthesis results for complex, irregular geometries (e.g., castles and cathedrals) to demonstrate the framework's robustness; (ii) a sensitivity analysis of refinement text prompts;(iii) an episode-vs-coverage analysis to quantify the effectiveness of the curriculum strategy; and (iv) synthesized results with different random seed.

Additionally, we provide an interactive HTML visualization (available in the folder, `main.html`) that allows readers to explore our video results and compare reconstructions across different viewing conditions and scenes. This visualization enables direct comparison of our method's geometric accuracy, spatial alignment, and overall perceptual quality against baseline approaches and Google Earth Studio reference video.

We also provide example datasets via Zenodo, which can be accessed at this URL. However, due to storage limitations, we only provide training data for an AOI as an example. We plan to release the complete dataset upon acceptance.

A.1 IMPLEMENTATION DETAILS

Codebase. Our method extends the Mip-Splatting (Yu et al., 2024) codebase with custom modules for satellite imagery processing and our curriculum-based IDU refinement pipeline.

Pseudo camera depth supervision. We sample cameras with varied azimuths and decreasing elevations, using random per-image embeddings. MoGe (Wang et al., 2024a) provides scale-invariant depth estimation. We sample 24 views every 10 iterations, with look-at points (x, y, z), where $x, y \sim \mathcal{N}(0, 128)$ and $z = 0$, as illustrated in Figure 10. Camera azimuths are uniformly sampled between 0 and 2π, while elevation angles and radii linearly decrease from 80° to 45° and 300 to 250 units, respectively. Rendered RGB images (I_{RGB}) are 1024×1024 pixels. We illustrate the 3DGS rendered RGB image I_{RGB}, scale-invariant depth D_{est} estimated by MoGe (Wang et al., 2024a) and depth from 3DGS D_{GS} in Figure 11.

3DGS reconstruction from satellite imagery. Our satellite-view optimization process runs for 30,000 iterations, with densification enabled between iterations 1,000 and 21,000. We modify several key parameters in the standard 3DGS implementation to address satellite imagery's unique challenges. First, to prevent undesirable Gaussian elongation artifacts common with overhead views, we reduce the scaling learning rate from 0.005 to 0.001. Second, we address sparsity issues of Gaussian points in close-up renderings by lowering the densification gradient threshold from 0.002 to 0.001, ensuring sufficient detail when viewed from ground level. Furthermore, we implement pruning of Gaussians with maximum covariance exceeding 20 to eliminate floating artifacts. The loss function weights are set to $\lambda_{\text{D-SSIM}} = 0.2$, $\lambda_{\text{op}} = 10$, and $\lambda_{\text{depth}} = 0.5$ for optimal reconstruction quality. For appearance modeling, we adopt the architecture from WildGaussians (Kulhanek et al., 2024), implementing an appearance MLP with 2 hidden layers (128 neurons each) and ReLU activation functions. The per-image and per-Gaussian embedding dimensions are set to 32 and 24 respectively, with learning rates of 0.001, 0.005, and 0.0005 for per-image embeddings e_j, per-Gaussian embeddings g_i, and the

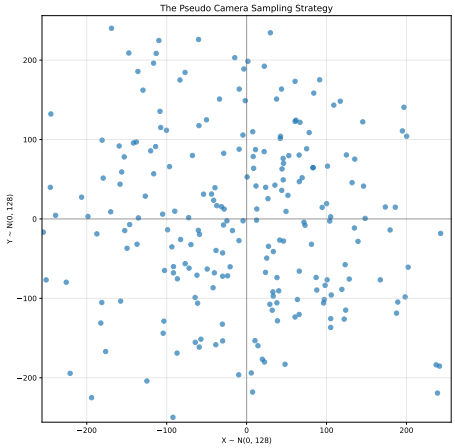

Figure 10: **The sampling strategy of pseudo camera.** In this example, we sample 240 points using the strategy.

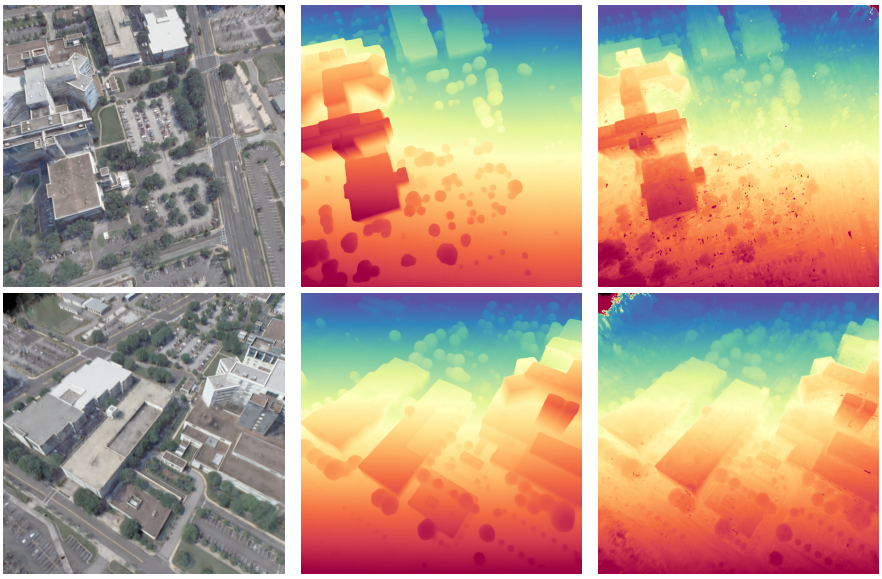

Render RGB I_{RGB} Estimated Depth D_{est} 3DGS Depth D_{GS}

Figure 11: **Pseudo-cam Depth Supervision.** We use MoGe (Li et al., 2024c) to estimate the scale-invariant depth D_{est} from the rendered RGB image I_{RGB}. The rightmost figures show the rasterized depth D_{GS} from 3DGS.

appearance MLP f, respectively. The complete satellite-view training requires approximately 1 hour on a single NVIDIA RTX A6000 GPU.

FlowEdit-based refinement. We set FlowEdit noise parameters $n_{\text{min}} = 4$ and $n_{\text{max}} = 10$ to balance artifact removal with detail preservation. Our source prompt ("*Satellite image of an urban area with modern and older buildings, roads, green spaces. Some areas appear distorted, with blurring and warping artifacts.*") characterizes initial renders, while the target prompt ("*Clear satellite image of an urban area with sharp buildings, smooth edges, natural lighting, and well-defined textures.*") guides refinement. These parameters were determined through experimentation, with lower noise values preserving more original structure but removing fewer artifacts, and higher values creating

more significant changes but potentially altering underlying geometry. All other FlowEdit parameters use default values.

Curriculum-based refinement details. Our IDU process comprises $N_e = 5$ episodes of 10,000 iterations each, with densification through iteration 9,000. At the start of IDU, we randomly select and fix a single per-image appearance embedding e_j. Opacity regularization is disabled during IDU, as our curriculum naturally mitigates floating artifacts through multi-view consistency, enabling Gaussians to retain variable opacities beneficial for semi-transparent structures (Kerbl et al., 2023). For DFC2019 (Le Saux et al., 2019) dataset, we utilize $N_p = 9$ look-at points in a 3×3 grid (512 units wide, centered at origin), with $N_v = 6$ cameras per point and $N_s = 2$ samples per view. Camera elevations decrease from $85°$ to $45°$ and radii from 300 to 250 units across episodes. For GoogleEarth (Xie et al., 2024) dataset, we utilize $N_p = 16$ look-at point at origin, with $N_v = 6$ cameras per point and $N_s = 2$ samples per view. Camera elevations decrease from $85°$ to $45°$ and radius is fixed 600-unit across episodes. All training images are rendered at 2048×2048 resolution. Our training strategy samples 75% from refined images and 25% from original satellite images, this sampling strategy makes sure that the final 3DGS scene faithfully follows the semantic and layout in the input satellite imagery. The complete synthesizing stage requires approximately 6 hours on a single NVIDIA RTX A6000 GPU.

Detail of training time. All time measurements were conducted on the JAX_214 AOI using a single NVIDIA RTX A6000 (48GB) GPU. The total training time increases from approximately 1 hour 35 minutes for the baseline reconstruction (30K iterations) to 6 hours 45 minutes for the full pipeline. The majority of this additional cost is attributed to the Curriculum-based Iterative Dataset Update (IDU) process (5 episodes), which accounts for approximately 5 hours and 10 minutes combined. Specifically, a single IDU episode requires roughly 1 hour, where the computational load is split almost evenly between render refinement ($\sim$30 min) and 3DGS reconstruction update ($\sim$32 min), while the initial rendering step is negligible ($\sim$4 s). While this results in a total training time increase of approximately $4.3\times$, we view this as a justifiable offline investment to bypass physical data collection limitations.

Detail of memory consumption. We distinguish between peak memory and final memory. The peak memory usage reaches 46 GB during the synthesis stage, driven by the overhead of loading the diffusion model (FLUX.1) and temporary densification of Gaussians. However, the final training memory footprint is significantly lower (28.04 GB) as our method actively prunes redundant and low-opacity points. In terms of scene complexity, the refinement process densifies the scene by approximately 27%, increasing the Gaussian count from $\sim$1.65 million (reconstruction stage) to $\sim$2.1 million, specifically targeting the vertical facade geometry missing in the initial satellite reconstruction.

Validity of RPC to perspective approximation. We adopt the methodology proposed in SatelliteSfM (Zhang et al., 2019) to approximate the satellite linear pushbroom sensor as a perspective camera. This approximation relies on the "weak perspective" assumption, which holds valid when the satellite altitude (Z) is significantly larger than the depth variation within the scene (ΔZ), i.e., $Z \gg \Delta Z$. Given that satellites orbit at distances of hundreds of kilometers while terrestrial depth variations are limited to a few hundred meters, the ratio $\Delta Z/Z$ remains negligible, allowing the geometry to converge to a perspective model. The approximation is achieved by generating a dense grid of 3D-2D correspondences using the rigorous RPC model and solving for a projection matrix P via the Direct Linear Transformation (DLT) method, which is subsequently decomposed ($P = K[R|t]$) to recover camera parameters. Quantitative evaluations demonstrate that this process introduces negligible error: the average maximum forward projection error against the rigorous RPC model is only **0.126 pixels**, and the difference in triangulated 3D points is typically less than **5 cm**. Furthermore, this initialization allows Bundle Adjustment to achieve sub-pixel accuracy, with median reprojection errors recorded at **0.864 pixels**, confirming the suitability of this approximation for high-fidelity 3D reconstruction.

A.2 Main Paper Experiments Detail & Results

DFC2019 (Le Saux et al., 2019) dataset details. The number of training images and geographical coordinates for each AOI is provided in Table 5. We also include four additional AOIs from

Table 5: **Number of training images and geographical coordinate per Area of Interest (AOI).** These AOIs correspond to standard evaluation scenarios established by previous works, ensuring consistent and fair comparisons with existing baselines (e.g., Sat-NeRF (Marí et al., 2022)).

AOI	JAX_004	JAX_068	JAX_214	JAX_260
# of training image	9	17	21	15
Geographical coordinate	81.70643°W, 30.35782°N	81.66375°W, 30.34880°N	81.66353°W, 30.31646°N	81.66350°W, 30.31184°N

Table 6: **Number of training images and geographical coordinates for additional AOIs.** We selected 4 additional AOIs with distinct characteristics: JAX_164 features a city hall building, JAX_175 contains an American football stadium, while the remaining two AOIs present other notable urban structures.

AOI	JAX_164	JAX_168	JAX_175	JAX_264
# of training image	20	21	21	21
Geographical coordinate	81.66362°W, 30.33032°N	81.65297°W, 30.33037°N	81.63696°W, 30.32583°N	81.65285°W, 30.31189°N

Jacksonville to demonstrate our method's robustness across varying scene characteristics. The number of training images and geographical coordinates for these additional AOIs is provided in Table 6. These additional AOIs feature distinct characteristics: one contains a city hall building (JAX_164), another includes an American football stadium (JAX_175), while the remaining two exhibit other notable urban features (JAX_168 and JAX_264).

GoogleEarth (Xie et al., 2024) dataset details. The GoogleEarth dataset, introduced by CityDreamer (Xie et al., 2024), contains semantic maps, height fields and renders from Google Earth Studio (Google, 2024) of New York City. This dataset is used to train the generative model in CityDreamer (Xie et al., 2024) and GaussianCity (Xie et al., 2025b). We pick four AOIs which contain diverse city elements, including complex architectures (`004`), squares (`010`), resident area (`219`) and riverside (`336`). However, original GES renders provided in GoogleEarth dataset are rendered from a lower elevation angle, which is not similar to satellite imagery. Therefore, for each AOI, we render 60 images from GES using an orbit trajectory with $80°$ of elevation angle and 2219 of radius. These new renders serve as the input of our methods. The AOI ID, geographical coordinates, and the number of input images are detailed in Table 7.

User study details. We asked participants three specific questions and instructed them to select one video that best addressed each question:

1. **Geometric Accuracy**: "Which video's 3D structures (buildings, terrain, objects) more accurately represent the real-world geometry when compared to the ground truth video?"
2. **Spatial Alignment**: "Which video's layout and positioning of elements better matches the satellite imagery reference?"
3. **Overall Perceptual Quality**: "Considering all aspects (geometry, textures, lighting, consistency), which video presents a more convincing and high-quality 3D representation of the scene?"

For the user study on DFC2019 dataset, each participant viewed videos from Sat-NeRF (Marí et al., 2022), our method without IDU, and our complete method, alongside Google Earth Studio reference footage and the original satellite imagery. For the user study on the GoogleEarth dataset, each participant viewed videos from CityDreamer (Xie et al., 2024), GaussianCity (Xie et al., 2025b) and our complete method, alongside Google Earth Studio reference footage and the reference satellite imagery.

Comparison details. For quantitative comparisons with Sat-NeRF (Marí et al., 2022), Mip-Splatting (Yu et al., 2024) and our method without IDU refinement, we used consistent camera parameters across all methods: $17°$ elevation angle, 328-unit radius, and $20°$ field of view, with cameras targeting the AOI's origin. For comparisons with CityDreamer (Xie et al., 2024) and GaussianCity (Xie et al., 2025b), we use $45°$ elevation angle, 1067-unit radius, and $20°$ field of view, with cameras also targeting the AOI's origin. These parameters were selected to ensure equitable comparison with similar scene coverage across methods.

Table 7: **Number of training images and geographical coordinate per Area of Interest (AOI).** We pick 4 AOIs from the GoogleEarth (Xie et al., 2024) dataset, ensuring fair comparisons with existing baselines (e.g., CityDreamer (Xie et al., 2024) and GaussianCity (Xie et al., 2025b))

AOI	4WorldFinancialCtr (004)	10UnionSquareE#5P (010)	219E12thSt (219)	336AlbanySt (336)
# of training image	60	60	60	60
Geographical coordinate	74.01587°W, 40.71473°N	73.98975°W, 40.73482°N	73.98690°W, 40.73187°N	74.01753°W, 40.71020°N

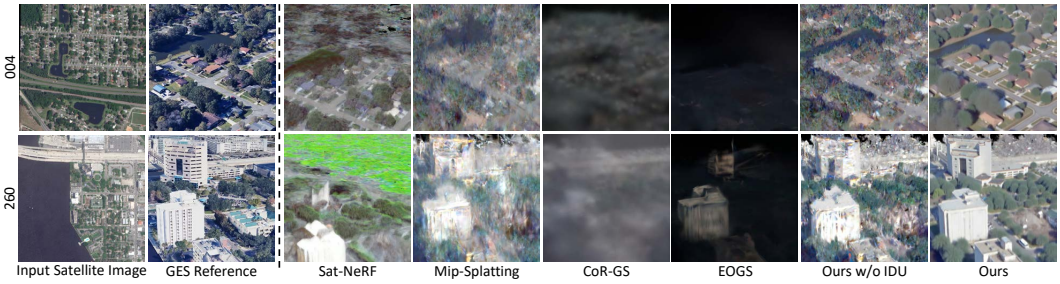

Figure 12: **Additional qualitative comparison on the DFC2019 dataset with Sat-NeRF (Marí et al., 2022), Mip-Splatting (Yu et al., 2024), CoR-GS (Zhang et al., 2024b), and EOGS (Savant Aira et al., 2025).** Our method significantly outperforms baseline approaches in both geometric accuracy and texture quality when rendering low-altitude novel views. Note the superior building geometry, facade details, and reduced floating artifacts in our final result.

Per-scene quantitative comparison. We provide per-scene quantitative comparison in Tables 8 and 9.

Additional qualitative comparisons. Due to space constraints in the main paper, we present additional qualitative comparison results in this supplementary material for scenes JAX_004 and JAX_260 from the DFC2019 dataset, and scenes 004 and 219 from the GoogleEarth dataset. Figure 12 shows orbital view comparisons with Sat-NeRF (Marí et al., 2022), Mip-Splatting (Yu et al., 2024), CoR-GS (Zhang et al., 2024b), and EOGS (Savant Aira et al., 2025), while Figure 13 presents city-scale view comparisons with CityDreamer (Xie et al., 2024), GaussianCity (Xie et al., 2025b), and CoR-GS (Zhang et al., 2024b). These additional results further demonstrate the consistent superiority of our method across diverse urban environments.

Additional visual results. We also provide qualitative results on four additional AOIs from Jacksonville to demonstrate our method's robustness across diverse urban environments. As shown in Figure 19 and Figure 20, these AOIs contain distinctive architectural features: JAX_004 showcases a residential area with mixed housing types and green spaces; JAX_164 features a prominent city hall building with its characteristic dome and symmetrical facade; JAX_175 encompasses an American football stadium with its distinctive oval structure and surrounding parking facilities; JAX_168 contains a commercial district with varied building heights and dense urban layout. Despite these varied urban typologies, our method successfully generates coherent three-dimensional renderings that preserve the spatial relationships and architectural features present in the satellite imagery. These additional results further validate the generalizability of our approach across diverse urban landscapes without requiring scene-specific parameter adjustments.

Multi-date appearance variation. The use of multi-date satellite imagery introduces a significant challenge, as images of the same location, when captured on different days, exhibit drastic variations in appearance. As shown in Figure 21, these differences can fundamentally alter the scene's geometry and texture. Effectively synthesizing novel views requires a model capable of intelligently disentangling the static 3D scene structure from these challenging, temporally-varying appearance factors.

A.3 Additional Experiments

Qualitative results on complex geometries. To demonstrate the robustness of our framework beyond standard city-block layouts, we evaluate our method on scenes featuring irregular and historically

Figure 13: **Additional qualitative comparison on the GoogleEarth dataset with CityDreamer (Xie et al., 2024), GaussianCity (Xie et al., 2025b), and CoR-GS (Zhang et al., 2024b).** Our method is able to synthesize texture and geometry that is closer to the reference GES render.

Table 8: **Quantitative comparison on each AOI of DFC2019 (Le Saux et al., 2019).** Our method consistently outperforms baseline methods on distribution metrics and most pixel-level metrics, indicating superior image synthesis quality. Metrics are computed between renders from each method and reference frames from GES.

		Distribution Metrics		Pixel-level Metrics*		
Scene	Methods	FID_{CLIP} ↓	CMMD ↓	PSNR ↑	SSIM ↑	LPIPS ↓
JAX_004	Sat-NeRF	79.97	3.838	11.95	0.2290	0.8700
	EOGS	107.23	5.913	8.22	0.1271	1.0174
	Mip-Splatting	85.33	4.986	13.06	0.2412	0.8157
	CoR-GS	91.01	5.131	11.25	**0.2554**	0.9793
	Ours	**24.45**	**1.474**	**12.90**	0.2446	**0.846**
JAX_068	Sat-NeRF	93.70	5.376	9.86	0.2607	0.8414
	EOGS	85.57	5.516	6.39	0.1593	0.9953
	Mip-Splatting	92.95	6.163	11.64	0.2900	0.8444
	CoR-GS	90.34	5.864	11.77	**0.3230**	1.0073
	Ours	**28.35**	**2.845**	**11.79**	0.2931	**0.8210**
JAX_214	Sat-NeRF	90.76	5.376	8.97	0.2684	0.8394
	EOGS	71.02	4.342	7.40	0.2293	0.8883
	Mip-Splatting	82.04	5.088	11.23	0.3844	0.8048
	CoR-GS	86.33	5.258	11.66	**0.4074**	0.9079
	Ours	**26.69**	**1.964**	**12.24**	0.3881	**0.7420**
JAX_260	Sat-NeRF	89.00	4.881	9.43	0.3172	0.9068
	EOGS	87.15	5.372	7.04	0.1574	0.9342
	Mip-Splatting	88.42	5.385	11.61	0.3579	0.8130
	CoR-GS	88.44	4.710	11.50	**0.4162**	0.8977
	Ours	**29.83**	**2.076**	**12.59**	0.3574	**0.7540**

significant architectures. As shown in Figure 20, we present synthesis results for **Neuschwanstein Castle** and **Wells Cathedral**. These scenes pose significant challenges due to their intricate non-Manhattan geometries, including sharp spires, varying elevations, and gothic architectural details. Despite these complexities, our method successfully disentangles the underlying geometry from the satellite input and hallucinates plausible high-frequency details for facades that are heavily occluded in the nadir views. This confirms that our hybrid reconstruction-generation approach is not limited to simple urban prisms but extends effectively to complex, free-form structures.

Synthesis of bridges. In addition to dense building clusters, we evaluate our method's performance on scenes with complex topological structures, such as bridges. Figure 16 illustrates renders of bridges in JAX_068, JAX_214 and JAX_175, a typically difficult case for standard photogrammetry due to the thin structural components. Our method successfully recovers the connectivity of the bridge span while synthesizing realistic water textures. The diffusion-based refinement effectively

Table 9: **Quantitative comparison with CityDreamer (Xie et al., 2024), GaussianCity (Xie et al., 2025b), CoR-GS (Zhang et al., 2024b) on each AOI of the GoogleEarth dataset (Xie et al., 2024).** The results show that our approach consistently achieves the best performance, indicating superior geometric and perceptual fidelity compared to all baselines. Metrics are computed between renders from each method and reference frames from GES.

		Distribution Metrics		Pixel-level Metrics		
Scene	Methods	$\text{FID}_{\text{CLIP}}\downarrow$	CMMD $\downarrow$	PSNR $\uparrow$	SSIM $\uparrow$	LPIPS $\downarrow$
004	CityDreamer	39.88	3.869	13.06	0.3519	0.5643
	GaussianCity	28.71	2.710	14.00	0.3786	0.5656
	CoR-GS	33.69	4.203	11.55	0.3440	0.6120
	Ours	**10.43**	**2.491**	**15.09**	**0.3793**	**0.3978**
010	CityDreamer	34.29	4.270	12.24	0.1387	0.5544
	GaussianCity	29.67	2.850	12.90	0.1661	0.5335
	CoR-GS	29.75	3.672	12.90	**0.1807**	0.4209
	Ours	**11.03**	**1.631**	**13.58**	0.1769	**0.4073**
219	CityDreamer	42.38	4.372	11.63	0.1344	0.5471
	GaussianCity	32.83	2.883	12.37	0.1676	0.5254
	CoR-GS	29.55	3.958	12.64	**0.1792**	**0.3974**
	Ours	**7.83**	**2.635**	**13.12**	0.1699	0.3975
336	CityDreamer	29.53	4.097	13.39	0.4431	0.5654
	GaussianCity	23.72	3.224	14.36	0.4533	0.5382
	CoR-GS	16.29	3.173	14.29	0.4592	0.3879
	Ours	**10.36**	**1.279**	**15.32**	**0.4662**	**0.3719**

regularizes the geometry, preventing the characteristic "melting" artifacts often observed in thin structures when using satellite-only reconstruction.

Visualizing transient object handling via per-image embeddings. A key challenge in multi-date satellite reconstruction is the handling of dynamic elements, such as moving vehicles and pedestrians, which can introduce ghosting artifacts. Our approach addresses this by learning per-image appearance embeddings e_j that capture photometric variations specific to each capture date. As visualized in Figure 14, rendering the same viewpoint across 20 distinct appearance embeddings reveals that transient objects exhibit significant variability, appearing clearly in some embeddings while fading or vanishing in others. This qualitative evidence suggests that our appearance modeling effectively acts as a "sink" for transient data that does not align with the static 3D geometry. By absorbing these inconsistencies into the appearance code rather than the geometric parameters, the optimization naturally disentangles transient elements from the underlying static structure, ensuring a clean and consistent geometric reconstruction.

Episode-vs-coverage analysis of curriculum strategy. To quantify the effectiveness of the IDU module in revealing occluded regions, we present an Episode-vs-Coverage analysis (Figure 18). Since ground truth 3D geometry is unavailable for these satellite scenes, we use the final converged 3DGS model as a proxy for the total scene surface. We compute the cumulative coverage by optimizing a visibility attribute for every Gaussian point against the camera poses utilized in each episode. As shown in the figure, the coverage ratio steadily increases from $\sim$0.50 in Episode 1 to $\sim$0.75 in Episode 5. This consistent gain confirms that our curriculum strategy, which progressively lowers camera elevation from 85° to 45°, successfully reveals and reconstructs vertical facade geometry that was initially occluded in the top-down satellite views. However, we acknowledge a limitation in this metric: because it calculates coverage based on reconstructed points, it cannot account for "true holes" (surface areas that were never generated at all because they were completely occluded from all sampled views). Future work could address this by dynamically sampling IDU cameras to target specific geometric uncertainties or detected holes.

Stochastic appearance diversity. To demonstrate the generative capacity of our hybrid framework, we evaluate the stochastic diversity of the synthesized textures in Figure 22. By varying the random seed during the diffusion refinement stage while maintaining the same geometric initialization, our

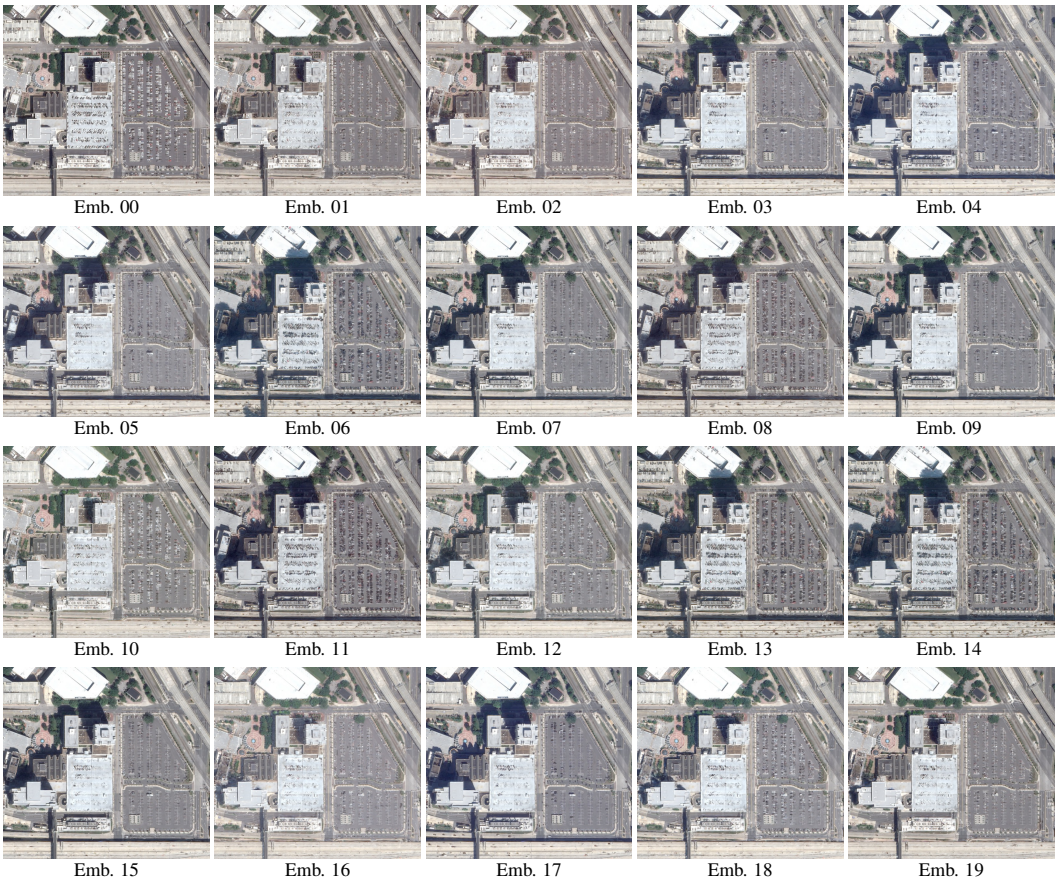

Figure 14: **Visualizing transient object handling via per-image embeddings.** We render the same viewpoint using 20 different learned appearance embeddings (Emb. 00–19). Observe that transient objects, such as the vehicles on the road, exhibit varying degrees of visibility across different embeddings (e.g., clearly visible in some, faded or absent in others), while the static building geometry remains consistent. This qualitatively demonstrates that our per-image appearance modeling effectively disentangles transient elements from the underlying static 3D structure, preventing dynamic artifacts from corrupting the geometric reconstruction.

method produces diverse yet plausible surface details for identical underlying structures, 5643]. As illustrated in the figure, detailed features such as the text on the red building signage vary distinctively (e.g., "Outeil" vs. "CUTAN"). Crucially, the macroscopic building footprint remains geometrically fixed, confirming that our framework successfully disentangles the reconstruction of physical geometry (grounded in satellite constraints) from the generative synthesis of high frequency appearance.

A.4 LLM Usage Disclosure

Large language models (LLMs) were used to assist in improving the clarity and conciseness of the writing and in searching for related work. All technical ideas, algorithm designs, experiments, and analysis were conceived, implemented, and validated by the authors. The authors have carefully verified all content and take full responsibility for the correctness and integrity of this paper.

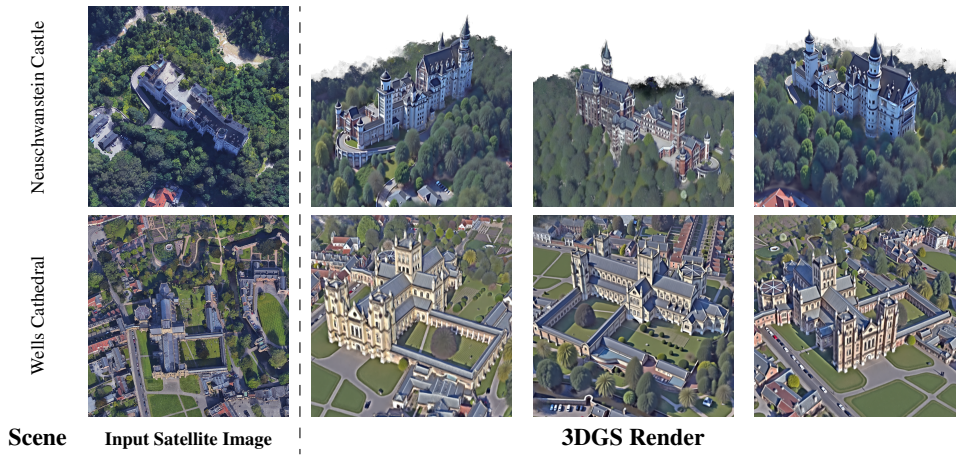

Figure 15: **Qualitative results on complex geometries.** Visualization of satellite image inputs and corresponding rendered frames. We demonstrate the model's capability on irregular historical architectures, including Neuschwanstein Castle and Wells Cathedral, showing the synthesis of complex geometry.

(a) JAX_068 (b) JAX_175 (c) JAX_214

Figure 16: **Qualitative results for bridges.** We present the render results for bridges appears in JAX_068, JAX_214 and JAX_175, demonstrating the method's ability to handle complex topological structures and water surfaces that are typically challenging for standard reconstruction pipelines.

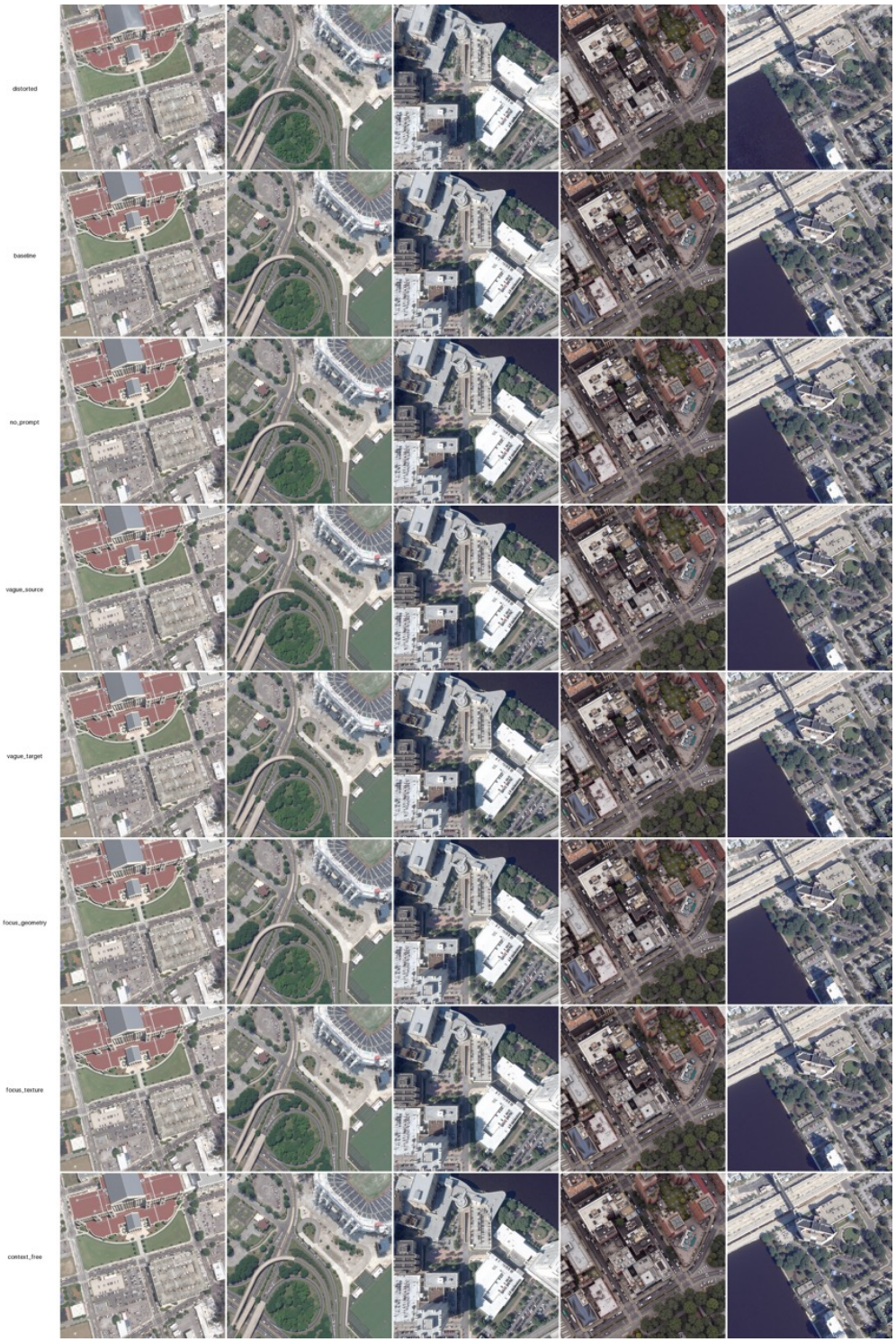

Figure 17: **Refine renders with different prompt strategies.**

Table 10: **List of text prompts used in sensitivity analysis.** We evaluate six different prompting strategies to test the robustness of our method.

Strategy	Source Prompt (P_{src})	Target Prompt (P_{tar})
Baseline	Satellite image of an urban area with modern and older buildings, roads, green spaces. Some areas appear distorted, with blurring and warping artifacts.	Clear satellite image of an urban area with sharp buildings, smooth edges, natural lighting, and well-defined textures.
Vague Source	A blurry satellite image of an urban area.	Clear satellite image of an urban area with sharp buildings, smooth edges, natural lighting, and well-defined textures.
Vague Target	Satellite image of an urban area with modern and older buildings, roads, green spaces. Some areas appear distorted, with blurring and warping artifacts.	A clear satellite image of an urban area.
Focus Geometry	Satellite image of an urban area with modern and older buildings, roads, green spaces. Some areas appear distorted, with blurring and warping artifacts.	Clear satellite image of an urban area with geometrically precise buildings, flat rooftops, straight edges, and well-defined roads.
Focus Texture	Satellite image of an urban area with modern and older buildings, roads, green spaces. Some areas appear distorted, with blurring and warping artifacts.	Clear satellite image of an urban area with realistic, high-resolution textures, detailed facades, clear vegetation, and natural lighting.
Context Free	distorted, blurring, warping artifacts	clear, sharp, smooth edges, natural lighting, well-defined textures

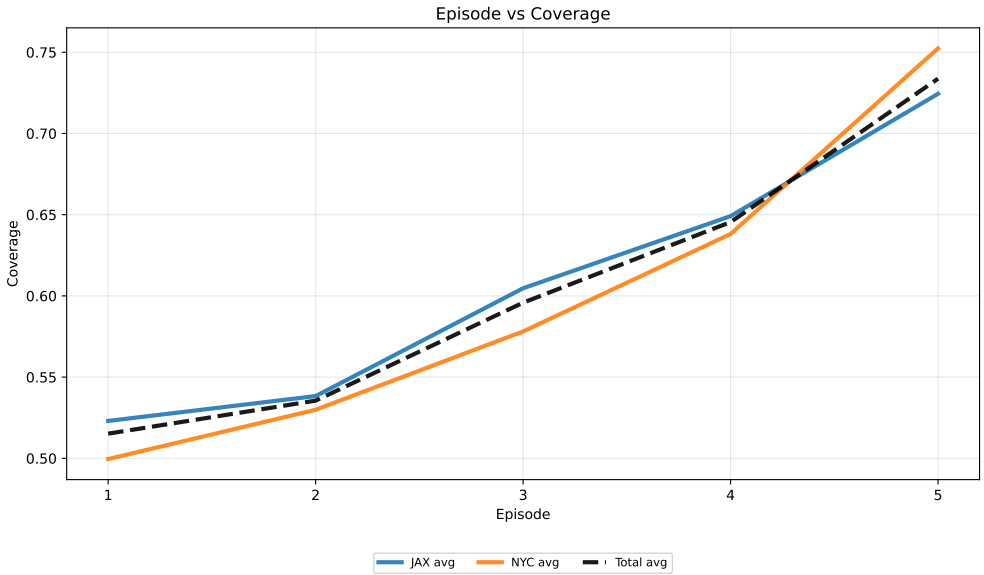

Figure 18: **Episode-vs-Coverage analysis.** The plot illustrates the cumulative surface coverage ratio increasing across refinement episodes. The curriculum-based strategy effectively exposes occluded regions, particularly vertical facades, as the camera elevation descends.

Figure 19: **Qualitative results across primary scenes.** Visualization of satellite image inputs and corresponding rendered frames for our four main AOIs.

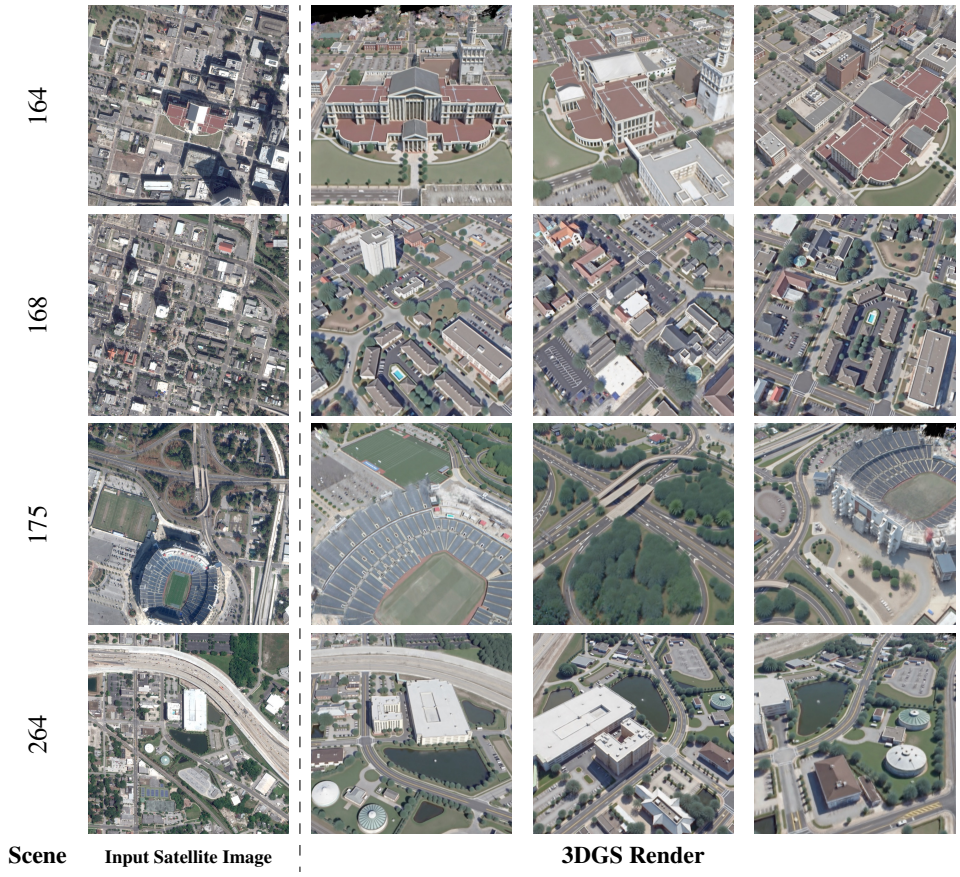

Figure 20: **Qualitative results across additional scenes.** Visualization of satellite image inputs and corresponding rendered frames for four additional AOIs with distinctive characteristics: JAX_164 features a city hall building, JAX_175 contains an American football stadium, while JAX_168 and JAX_264 present other notable urban structures.

Figure 21: **Visualization of multi-date satellite imagery of the DFC2019 dataset.** Note the substantial shifts in appearance, including changes in illumination, cloud cover, and surface characteristics, which introduce challenges for consistent 3D reconstruction.

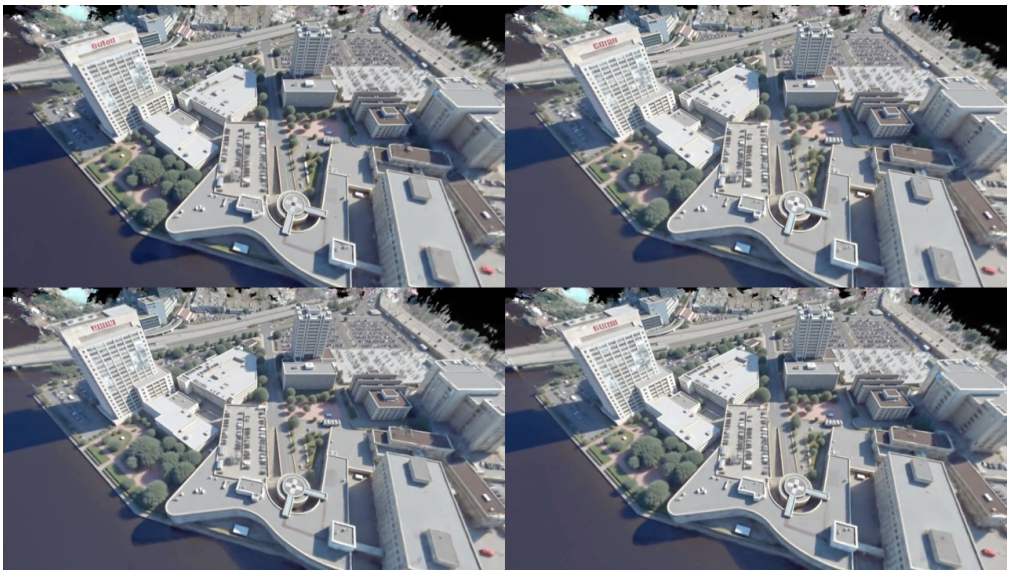

Figure 22: **Demonstration of stochastic appearance diversity while preserving geometric consistency.** Our method generates diverse plausible textures for identical underlying geometry across different random seeds. Notice how the red signage text on the building facade varies distinctively (e.g., “Outeil” vs. “CUTAN”) while the building’s structural footprint remains fixed, confirming that our framework successfully disentangles geometric reconstruction (grounded in satellite data) from generative appearance synthesis (variable via diffusion).